EFFECTS OF PROCESS CONDITIONS ON POLYMER NETWORK FORMATION

EFFECTS OF PROCESS CONDITIONS ON POLYMER NETWORK FORMATION: APPLICATION IN PARTICLE COATING AND MODELING USING MOLECULAR DYNAMICS

By SHIMIAO ZHANG, B. ENG.

A Thesis Submitted to the School of Graduate Studies in Partial Fulfilment
of the Requirements for the Degree
Master of Applied Science

Master of Applied Science (2016) McMaster University

(Chemical Engineering) Hamilton, Ontario

TITLE: Effects of Process Conditions on Polymer Network Formation: Application in Particle Coating and Modeling Using Molecular Dynamics

AUTHOR: Shimiao Zhang, B. Eng.

SUPERVISOR: Dr. Li Xi (McMaster University)

NUMBER OF PAGES: xii, 83

Abstract

Cross-linked polymers are of great importance to industrial practice and theoretical studies. The unique network structures of these materials have endowed them with many superior properties. In this thesis, we study cross-linked polymers from both of experimental and theoretical sides, with an emphasis on the formation process and properties of the prepared networks. Two specific problems are investigated: development of polymer coatings over solid particles with *in situ* curing, and molecular dynamics (MD) study of network formation kinetics and structure-property relationship.

In the study of polymer coating, a hot-melt coating process for solid particles is developed. Phenolic resin is used to coat the substrates and subsequently cured *in situ*. Among various processing parameters, temperature is found to play an especially important role in the coating performance. Higher temperature leads to stronger coating layers with better barrier properties, whereas lower temperature is preferable for better surface morphology. These two trends can be partially reconciled with ramping temperature profiles; however, the improvement is eventually limited by the rate of heat transfer.

In MD study, the effects of precursor topology on the formation, structure and mechanical properties of polymer networks are studied. Cross-linked polymer networks are synthesized from three sets of precursors with varying chain length. Little difference is observed between these networks in typical properties including radial distribution function, overall statistics of network connectivity, and glass transition behaviors. The elastic modulus of

the network is found to correlate strongly with the number of elastic strands in the network, except at the highly-cross-linked limit where substantial discrepancy is observed between networks from different precursors. Although these final networks contain a similar level of structural defects, the choice of precursor has a significant effect on the spatial distribution of the defects, which explains the precursor dependence of their mechanical property observed in the tensile test.

Acknowledgments

First and foremost, I would like to express my sincere thanks and heartfelt gratitude to my supervisor, Dr. Li Xi, for providing me with the opportunity to explore the simulation world and research on polymers. This thesis would not be possible without his patient guidance and continual encouragement throughout the past two years. I would also like to acknowledge the Natural Sciences and Engineering Research Council of Canada (NSERC) for financial support of the projects, and the Shared Hierarchical Academic Research Computing Network (SHARCNET) and Compute/Calcul Canada for the facilities used to run computational tasks.

I also hope to take this opportunity to thank Dr. Santiago Faucher and Lai Chi So for many inspiring discussions and insightful suggestions they have provided on the study of polymer coatings. Special thanks to the technical staffs for their assistance during this study: Paul Gatt for the fabrication of crush test cell and impellers, and Kent Wheeler for the training and use of the hydraulic load frame in Applied Dynamics Laboratory.

I am also thankful to the former and current members of Dr. Li Xi's research group who I have enjoyed working with, and to all of my friends at McMaster University, whose friendship has made my experience here unforgettable.

Finally, I would like to thank my family for their unconditional love and endless supports over these years. No word can fully express my gratitude and appreciation.

Table of Contents

List of Figures

List of Tables

List of Abbreviations and Symbols

MD	Molecular dynamics
PLD	Pulse laser deposition
γ-GPS	γ -glycidoxypropyltrimethoxysilane
MeOH	Metal hydroxyls
HMTA	Hexamethylenetetramine
CT	Constant temperature
RT	Ramping temperature
DSC	Differential scanning calorimeter
TGA	Thermogravimetric analysis
SEM	Scanning electron microscopy
MC	Monte Carlo
MM	Monomer-monomer
LM	Long chain-monomer
SS	Short chain-short chain
LJ	Lennard-Jones
U_{lj}	Lennard-Jones potential
r	Distance between particles in simulation box
r_c	Cut-off distance
ε	LJ unit of energy
σ	LJ unit of distance
FENE	Finite extension nonlinear elastic
U_{FENE}	FENE potential
k	Spring constant of FENE potential, $30\varepsilon/\sigma^2$
R_0	Maximum bond length, 1.5σ
τ	LJ unit of time
Δt	Time step, 0.005τ
m	LJ unit of mass
k_B	Boltzmann constant
T	Reduced temperature, ε/k_B
LAMMPS	Large-scale Atomic/Molecular Massively Parallel Simulator
DPD	Dissipative particle dynamics
U_{soft}	Cosine soft potential
A	Amplitude of cosine soft potential
U_{DPD}	DPD soft potential
a_{DPD}	Maximum repulsion parameter of DPD soft potential
Tg	Glass transition temperature
NPT	Isothermal-isobaric ensemble
P	Reduced pressure
$\dot{e}$	Constant true strain rate

L	Simulation box length
L_0	Initial box length (before tensile deformation)
σ_{ts}	Tensile stress
P_x	Tensile stress at x direction
P_y	Tensile stress at y direction
P_z	Tensile stress at z direction
ϵ_{ts}	Tensile strain
Mw	Weight-averaged molecular weight
RDF	Radial distribution function
PDF	Probability density function
HPC	High performance computing

Chapter 1

Overview: the scope of study

Cross-linked polymers have been the focus of study in various areas for many years. These materials are composed of a three-dimensional network of multiple repeating units which are interconnected with one another, endowing them with superior performance.[1] One of the typical materials in this class is vulcanized rubber.[2, 3] Compared to the unvulcanized raw materials (e.g., natural rubber), vulcanized rubbers show many desired properties including improved elasticity and modulus, and impermeability to liquids and gases, enabling their wide applications in industry such as manufacture of automobile tires, flexible tubing and stoppers, *etc*.[4] Another example of cross-linked polymers is cured thermosetting resins (e.g., phenolic resins and epoxy resins) which have been extensively used in paints and coatings, adhesives, and composite materials.[5, 6] Despite their extensive applications and long history of use, there are still various unsolved issues associated with cross-linked polymers. Structure-property relationship of networks[7, 8] and cross-linking mechanisms[9] are a few examples for the existing problems of interest to many researchers.

As indicated by the title of this thesis, we study the cross-linked polymers in two different areas. Specifically, we are interested in the development of polymer coatings over solid particles with *in-situ* curing, and the use of MD technique to provide more insights into the formation and structure-property relationship of polymer networks. Our interest in polymer coating of three-dimensional substrates is largely motivated by their applications in hydraulic fracturing (fracking) operations, in which resin-coated particles are used as proppants and injected with pressurized fluids into the well to prop open the produced cracks.[10] Compared with coating on flat surfaces, coating of three-dimensional objects with *in-situ* curing is more complicated, which involves a complex coupling of different processes including polymer rheology, mass and heat transfer, and curing reaction. Our goal is to investigate the dependency of the competition profiles of these simultaneous processes on various operating parameters, and develop an optimized coating strategy for the best coating outcome. In addition, we do not limit the study to explore the relationship between the process conditions and resultant coating performance, but also aiming to provide insights into the multiple physical and chemical processes underlying the coating process, with the hope that the strategies demonstrated in our current contribution can be generalized to other applications of polymer coatings where multiple simultaneous processes are present.

Based on our experimental observations, the competition profiles of the multiple processes mentioned above are found to play a crucial role in determining the coating outcome. An essential understanding of how such competition depends on the process conditions is thus significant. Solving this issue from experiments is however non-trivial---while we need

various parameters (e.g., diffusion of cross-linkers, curing kinetics) to track and understand the whole process, they are actually not easy to access due to their complex dependence on each other.

In the other hand, computer simulation techniques have been proven a powerful tool in studying polymer materials.[11] These techniques form a bridge between experimental and theoretical research, which can provide valuable supplements to experiments (e.g., diffusion of small molecules in polymer systems[12, 13]) while allowing a detailed examination of theoretical models (e.g., reptation model for motions of long linear polymer chains[14] and rubber elasticity theory[15]). Among various techniques, MD simulation has been shown to be useful in studying dynamics of molecules, as it can provide a temporal evolution of the studied systems. We thus resort to MD technique to investigate the fundamental issue raised form our experimental study, as discussed above. However, the first challenge we need to confront is to build an appropriate molecular model of polymer network. Similar to real experiments in which cross-linked polymers can be synthesized from different polymerization processes and precursors, molecular models of polymer networks can also be generated in many ways, ranging from different cross-linking procedures to varying choices of precursors. However, there is not any standard or recommended way to develop the network models, and a fundamental understanding of the effects of preparation methods on the polymer networks is also not available. Studies focusing on this issue is very limited except a few past studies showing that the rigidity of precursor chains and choices of cross-linkers are indeed the concern when preparing polymer networks.[16, 17] In our study, we hope to shed some light on this issue: we prepare

polymer networks from different precursors with varying chain length and try to find difference among these materials in terms of their formation, structure and properties. Chain length of precursors is a more common variable which is usually selected randomly and varies significantly among different studies. The purpose of this work is to understand the effects of precursor topology on the synthesized networks and provide a guidance in developing molecular models of polymer networks from different precursors. While the current study does not provide a direct answer for the questions raised from our experiments, it serves as a basis for the development of an appropriate molecular model of polymer networks which will be used in our future studies.

The following content of this thesis is therefore divided into two separated parts. In part I, we present our study on polymer coatings over solid particles, while part II is for MD study of polymer networks. For each part, we provide an introduction for the field of study, a description of employed methodologies, discussions of results, conclusions of the work and a brief proposal for the future studies. Though our contributions are only limited to a specific problem of the field of interest, the new insights we have provided in each study have potential influences on the related areas.

Bibliography

(1) Aharoni, S. M. *Synthesis, characterization, and theory of polymeric networks and gels*; Springer Science & Business Media, 1992.

(2) Kohjiya, S.; Ikeda, Y. *Chemistry, manufacture and applications of natural rubber*; Woodhead Publishing, 2014.

(3) Mark, J. E.; Erman, B.; Roland, M. *The science and technology of rubber*; Academic press, 2013.

(4) Vergnaud, J.-M.; Rosca, I.-D. *Rubber curing and properties*; CRC Press, 2016.

(5) Ellis, B. *Chemistry and technology of epoxy resins*; Springer, 1993.

(6) Gardziella, A.; Pilato, L. A.; Knop, A. *Phenolic resins: chemistry, applications, standardization, safety and ecology*; Springer Science & Business Media, 2013.

(7) Jin, J.; Yang, S.; Bae, B.-S. Network structure-property relationship in UV-cured organic/inorganic hybrid nanocomposites. *Polymer Chemistry* **2011**, *2*, 168.

(8) Shibayama, M. Structure-mechanical property relationship of tough hydrogels. *Soft Matter* **2012**, *8*, 8030.

(9) Fairbanks, B. D.; Scott, T. F.; Kloxin, C. J.; Anseth, K. S.; Bowman, C. N. Thiol-Yne photopolymerizations: novel mechanism, kinetics, and step-growth formation of highly cross-linked networks. *Macromolecules* **2008**, *42*, 211.

(10) Zoveidavianpoor, M.; Gharibi, A. Application of polymers for coating of proppant in hydraulic fracturing of subterraneous formations: A comprehensive review. *Journal of Natural Gas Science and Engineering* **2015**, *24*, 197.

(11) Binder, K. *Monte Carlo and molecular dynamics simulations in polymer science*; Oxford University Press, 1995.

(12) Sok, R.; Berendsen, H.; Van Gunsteren, W. Molecular dynamics simulation of the transport of small molecules across a polymer membrane. *The Journal of Chemical Physics* **1992**, *96*, 4699.

(13) Sonnenburg, J.; Gao, J.; Weiner, J. Molecular dynamics simulations of gas diffusion through polymer networks. *Macromolecules* **1990**, *23*, 4653.

(14) Kremer, K.; Grest, G. S.; Carmesin, I. Crossover from rouse to reptation dynamics: a molecular-dynamics simulation. *Physical Review Letters* **1988**, *61*, 566.

(15) Rottach, D. R.; Curro, J. G.; Budzien, J.; Grest, G. S.; Svaneborg, C.; Everaers, R. Permanent set of cross-linking networks: Comparison of theory with molecular dynamics simulations. *Macromolecules* **2006**, *39*, 5521.

(16) Hosono, N.; Masubuchi, Y.; Furukawa, H.; Watanabe, T. A molecular dynamics simulation study on polymer networks of end-linked flexible or rigid chains. *The Journal of Chemical Physics* **2007**, *127*, 164905.

(17) Tsige, M.; Stevens, M. J. Effect of cross-linker functionality on the adhesion of highly cross-linked polymer networks: a molecular dynamics study of epoxies. *Macromolecules* **2004**, *37*, 630.

Part I

Polymer Coatings over Solid Particles with *In Situ* Curing

Chapter 2

Introduction

Inorganic and organic coating technologies are extensively used for the purpose of surface protection, decoration, and functionalization.[1] Compared with coating on flat surfaces,[2] coating of three-dimensional objects, such as solid particles or granular materials, has been much less studied. Our interest in these materials is particularly motivated by their application in hydraulic fracturing (fracking) operations.[3] During fracking operations, a highly pressurized liquid mixed with additives is pumped into the well to induce the fracturing of the surrounding rock formations. These cracks provide pathways for the release of oil or gas locked behind the formations, allowing the exploitation of reservoirs inaccessible to conventional oil recovery techniques. Small granules, also known as proppants, are injected with the fluid, which stay in the cracks and hold them open after the pressure is removed. Ideal proppants should have sufficient mechanical strength and chemical stability to sustain the high pressure and acidity of the downhole environment. Meanwhile, cost is often also a crucial consideration. Common choices for proppants include river sands, walnut hulls, glass beads, and many other synthetic particles, such as sintered bauxite and ceramics.[4-6] Proppants coated with one or more resin layers are also being developed for enhanced resistance to chemicals and high closure pressure and better proppant flowback control.[5] Flowback of proppants after hydraulic fracturing is an

undesired process in which the particles flow out of the fractured zones and enter the wellbores with the produced fluids, leading to reduced well productivity and damage to production equipment.[7, 8] The resin coating layers not only serve as protective shells for the proppants, but also provide grain-to-grain bonding interactions that prevent their flowback. In the event of proppant crushing, these layers also act as cages to encapsulate the crushed fines. All of these lead to improved well productivity.[4, 5] Meanwhile, compared with the proppant substrate, which often comes at little to no cost by itself, resins are much more expensive, and their usage can significantly drive up the overall cost.[6, 9] Excessive resin usage also causes environmental concerns, as it may detach from the proppants, decompose, and chemically contaminate the surrounding soil and water sources.[10, 11] It is thus important to minimize the resin dosage in proppant coating processes. Coating of solid particles of similar sizes (micron to millimeter) also finds applications in many other fields, such as polymer-coated drug particles for controlled drug release,[12, 13] titania-coated glass beads for wastewater treatment,[14] chitosan-coated perlite beads for heavy metal adsorption,[15, 16] and resin-coated metallic cores for ion-exchange applications.[17]

Coating performance is determined by a range of factors, including the rheology of the coating materials, substrate surface properties, curing reaction kinetics (if introduced), and coating technique.[18-20] For solid particles, common coating methods include dip coating,[21] pulse laser deposition (PLD),[22, 23] and spray coating with fluidized beds.[12, 13, 24, 25] Chemical cross-linking or curing is often induced during or after the coating process for enhanced coating-layer properties. Although curing can be triggered by multiple means,[26-29] heat-induced or thermal curing remains the most widely used. At least for flat surfaces, coating

processes incorporating thermal curing have been studied for various polymer coating materials, such as epoxies, polyurethanes, silicones, and polyimides.[28, 29] Over the years, much effort has been dedicated to understanding the effects of operating parameters, such as curing temperature and curing time, on the outcome of the coating.[30-34] Lee et al.[35] prepared epoxy-based and polyurethane-based coatings on glass plates by means of powder coating. The development of the coating surface structure was found to depend both on the conversion of the curing reaction and on the isothermal complex viscosity of the coating layer. Also, for the powder coating of epoxy-based systems, Barletta et al.[36] found that although the film morphology was insensitive to baking temperature and was determined at the early stage of curing, the mechanical properties of the film depend strongly on both the baking temperature and the curing time, through which the degree of cross-linking was controlled. Yang et al.[37] studied the formation kinetics and reaction mechanism of the γ-glycidoxypropyltrimethoxysilane (γ-GPS) film on a metal surface. They demonstrated that the competition between two reactions, silanol–silanol condensation and silanol-metal hydroxyls (MeOH) reaction, resulted in a complex film formation process. The effects of multireaction curing kinetics were also the subject of a number of other studies.[38, 39]

Despite the extensive research on flat-surface coating processes, there has been no previous scientific study on the coating of three-dimensional objects, such as particles, with *in situ* curing. Compared with flat surfaces, coating of particles involves complex mixing and heat transfer processes, which, when coupled with curing kinetics, makes the coating outcome much more challenging to control. In the oil and gas industry, the hot-melt process[40] is often used for preparing resin-coated proppants, in which resin is mixed with the proppants

at a temperature higher than its melting point and curing is induced *in situ* through the addition of cross-linking agents.[41-43] Other techniques are also used, such as a solution batch mixing method (where proppants are dispersed in a resin solution and later dried) and on-the-fly coating (where proppants, together with the resin and a surface active agent, are suspended in a stream of gelled aqueous carrier for continuous coating).[44, 45] However, these methods are primarily applied for "on-site" coating (proppants are coated during the hydraulic fracturing process) and require the use of solvents. In this study, we select the more widely applicable hot-melt coating process and systematically investigate the effects of various operating parameters on the coating performance, which to the best of our knowledge has not been reported in the literature. The goal is to develop a low-cost and efficient method for polymer coating over solid particles. In addition to establishing the relationship between operating parameters and coating performance, the study also aims to provide insight into the intricate physical and chemical processes that underlie the coating process and determine its outcome. Although proppant coating is our main focus, the strategy demonstrated in this study can be generalized to a broad range of applications where particle coating with *in situ* curing is desired.

Chapter 3

Experimental Section

3.1 Materials

Proppants comprised of metal oxides, with a size ranging from 0.4 mm to 0.8 mm (between 20 and 40 mesh), and with assorted shapes (from near-spherical to angular) were used as received from Hatch Ltd. Durez 34358 novolac phenol-formaldehyde pastille resin was used as received from Durez Corporation. Hexamethylenetetramine (HMTA, ≥99.0%) and ammonium hydrogen difluoride (NH_4HF_2, ≥98.5%) were used as received from Sigma-Aldrich. Hydrochloric acid (HCl, 36.5%-38.0%) was used as received from Caledon Laboratories Ltd. Deionized water (DI water) was used for all solutions.

3.2 Resin Coating Processes

The performance of two coating processes was investigated. The schematics of the processes are shown in **Figure 3.1**. Both of them used the same experimental setup and followed similar procedures, except that one kept the coating temperature constant (**Figure 3.1a**) whereas the other used a ramping temperature profile (**Figure 3.1b**). A batch size of 100 g of proppants was used for all coating experiments. The proppants were dried in an oven overnight before being transferred to a preheated reactor vessel (**Figure 3.1c**). The

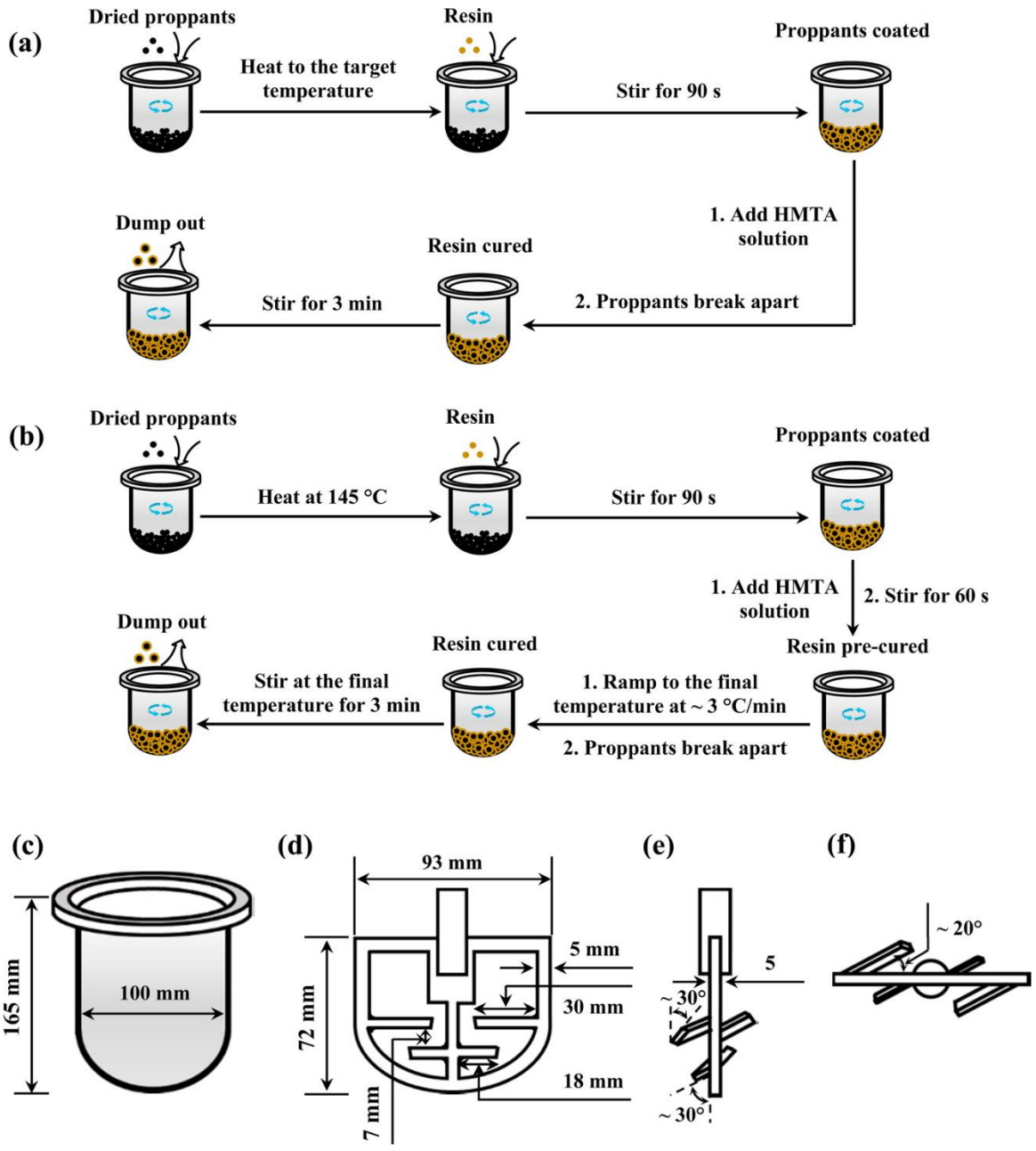

Figure 3.1. Schematics of the coating processes and apparatus: (a) constant temperature process, (b) ramping temperature process, (c) reactor vessel and the impeller design [(d) front view, (e) left view, and (f) bottom view].

vessel was heated with a heating mantle, and its temperature was measured with an infrared temperature gun. The samples were stirred with an impeller (**Figure 3.1d-3.1f**) throughout

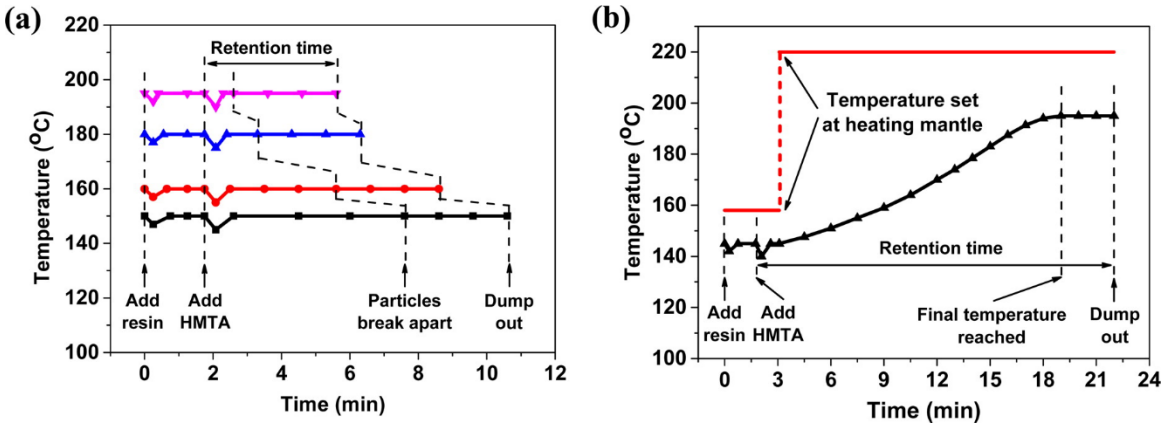

Figure 3.2. Temporal temperature profiles of the coating processes: (a) CT process (150 °C, 160 °C, 180 °C, and 195 °C) and (b) RT process; symbols represent real-time measurements during typical processes.

the process. In the constant temperature (CT) process (**Figure 3.1a**; corresponding temperature profiles are shown in **Figure 3.2a**), once the proppant temperature reaches the target value, resin pastilles (resin-to-proppant weight ratio of 1.6% or 3.3%) were added over 15 s, which quickly melt after contacting with the hot proppant surface, and led to a decrease in temperature of ~3 °C. Another 90 s was allowed for the temperature to stabilize and resin melt to distribute over the particles surface. HMTA solution (35% w/w in DI water) was then added to cure the resins, causing the temperature to drop by ~5 °C; a dry HMTA to resin weight ratio of 12% was used (higher HMTA dosage was tested with no significant influence on the results). The temperature was maintained at the target value for the rest of the process. As curing proceeded, the resin turned from a viscous fluid to a dry solid, after which the coated particles began to break apart from one another. The products were stirred for an additional 3 min (i.e., final holding stage) before they were discharged from the reactor and cooled down to room temperature. A 16-mesh sieve was then used to

screen the coated particles to remove the agglomerates. The ramping temperature (RT) process is similar except that the temperature started at 145 °C and was gradually increased to a higher final temperature after HTMA was introduced (**Figure 3.1b**). As shown in **Figure 3.2b**, 1 min after the addition of HMTA, a step change is imposed on the temperature of the heating mantle, which is raised to 220 °C (higher than the target temperature in the vessel). It takes about 16 min for the system temperature, measured at the center of the vessel, to reach the target final value, after which the system is held at this temperature for an additional 3 min. The spatial temperature distribution is nearly uniform at different stages: we have compared the measurements at different radial positions, and the variation (<2 °C) is smaller than the equipment error. We define the retention time of the curing process as the time from HMTA addition to the end of the process. For the CT process, it varies with the system temperature---from ~3.5 min at 195 °C to ~8.5 min at 150 °C: it takes longer time for the particles to break apart when temperature is lower. The retention time is much longer (~20 min) for the RT process, which we will further discuss below, owing to the time required for the system to reach the target final temperature. Both processes do not require specialized equipment and can be readily scaled up for low-cost, high-efficiency mass production. HMTA solution can be added either in droplets (using a pipet) or as a fine mist (using a spray bottle). Our experiments showed no noticeable difference in the resulting coating quality between the two methods.

Efficient stirring is crucial to avoid particle aggregation. Through repeated trials and errors, we have come to an impeller design (**Figures 3.1d-3.1f**) that essentially eliminates aggregation. Several features in this design were found to be particularly important. First,

the impeller size matches the inner diameter of the vessel (**Figure 3.1c**), which eliminates the dead regions of mixing and prevents the particles from sticking to the wall. Second, the large hollow area on the blade surface allows particles to pass through and avoids particle aggregation to the impeller surface. Third, four horizontal slabs extend into the hollow, which increases the tangential shearing rate between particles in the bulk and prevents their aggregation. The slabs are twisted out of the plane (by ∼30°, see **Figure 3.1e**) to allow particles to slide over as the impellor turns. The stirring rate used here was 350 rpm; the corresponding shear rate generated in the granular mixture is estimated at ∼40 s^{-1}, which was sufficient to efficiently mix the proppants with the resin and prevent particle–particle aggregation during the coating process. A further higher stirring rate will lead to the splashing of the particles. Under our current conditions, the amount of agglomerates was less than 1 wt %.

3.3 DSC Measurements

Differential scanning calorimeter (DSC) measurement was conducted to study the kinetics of the curing reaction between phenolic resin and HMTA using Q20 DSC equipment (TA Instruments, DE, USA). To prepare the sample, 6.2 mg of HMTA and milled resin, with an HMTA-to-resin weight ratio of 12%, was loaded into an aluminum crucible and dried in a desiccator before measurement. Temperature scan was performed at a heating rate of 10 °C/min. Nitrogen atmosphere was used with a gas flux rate of 50 mL/min.

3.4 TGA Measurements

Thermogravimetric analysis (TGA) was performed on coated proppants to determine the amount of resin applied onto the proppant surface. TGA was performed with a Q5000 IR TA Instruments (TA Instruments, DE, USA) appartus at a heating rate of 15 °C/min under air environment. Each proppant sample was held at 102 °C for 5 min to ensure removal of water before proceeding to higher temperatures.

3.5 SEM Imaging

A Tescan Vega II LSU scanning electron microscopy (SEM) (Tescan USA Inc., PA, USA), operating at 15.0 kV, was used to inspect the surface morphology of the uncoated and resin-coated proppants. Samples were fixed onto aluminum specimen stubs using carbon paints and coated with a gold layer by means of sputter coating in a Polaron E5100 coating unit (Polaron Instruments Inc., Watford, England) prior to SEM imaging.

3.6 Resin Coating Performance Characterization

Two characterization methods were used to quantify resin coating performance in the context of fracking application: (1) the acid solubility test measures the effectiveness of the resin coating in shielding the proppants from chemical leaching, and (2) the crush resistance test measures its capability in maintaining the structural integrity of proppants under high pressure. For both methods, explained in detail below, industrial standard protocols[46] are followed. Despite their roots in the oil and gas industry, the outcomes of these tests directly reflect coating-layer properties of general interest, such as its surface coverage (both tests), barrier property (acid solubility test), and mechanical strength (crush resistance test).

3.6.1 Acid Solubility Test

The acid solubility test measures the amount of weight loss in proppants after their exposure to a strong acid solution. Uncoated proppants are chemically unstable in acidic environments, for which the resin coating provides a protective layer. Performance in this test thus directly depends on the coating-layer coverage and its barrier property, i.e., resistance to acid permeation, which depends on the cross-linking density.[47] We follow the procedure given by the American Petroleum Institute Recommended Practice 19C (API RP 19C).[46]

An acid solution containing 12% HCl and 3% HF is prepared by mixing the appropriate amounts of solid NH_4HF_2, 37% HCl solution, and DI water. For the solubility test, 5 g of proppant samples was dried at 105 °C and then cooled down to the room temperature. The samples were added into a plastic beaker containing 100 mL of the acid solution. The beaker was then sealed to prevent the acid from evaporation and placed in a 66 °C water bath for 30 min without stirring. The acid solution was removed after the test via vacuum filtration and the retained solids were washed with 20 mL of DI water for three times. The solid sample was then dried at 105 °C until its weight levels off. The acid solubility was measured by the percentage mass loss of the sample compared with its initial weight.

3.6.2 Crush Resistance Test

The crush test measures the amount of crushed fines generated after a high pressure is applied onto the proppants. This crush resistance property depends on the coating-layer

coverage and the mechanical strength of the coatings which is affected by the degree of cross-linking as well.[36, 48] The procedure for this test also follows the recommendation in API RP 19C.[46]

The proppants were sieved using a 20/40 mesh sieve stack, comprising of a 20-mesh brass sieve on the top, a 40-mesh brass sieve in the middle, and a pan at the bottom. A test cell and piston were prepared in accordance to the recommendations outlined in API RP 19C. The sample, which weighs at 35.1 g, was loaded into the test cell and the piston was then gently placed on top of the sample. The sample surface was smoothed by rotating the piston 180° clockwise once. The test cell together with the piston was placed on a hydraulic load frame. A load was exerted onto the test cell and piston at a rate of 2000 pounds per square inch (psi) per minute until a final stress of 15,000 psi was reached. The final stress was held for 2 min before release. The crushed sample was sieved using the 20/40 mesh sieve stack. The material passing the 40-mesh sieve and that ended on the pan was weighed. Crush resistance was reported as the percentage of the original sample mass that ended up on the pan.

Chapter 4

Results and Discussion

4.1 Resin Curing Reaction

The curing reaction between the novolac phenolic resin (un-cross-linked precursors) and hexamethylenetetramine (HMTA) is highly complex. Its mechanism is not fully understood,[49-52] but it can be generically depicted by **Figure 4.1**. It is believed to consist of two stages: various intermediates, mainly benzoxazines and benzylamines, are first formed, before they are further cross-linked into a network.[49]

DSC was utilized to study the curing kinetics of phenolic resin and HMTA. As shown in **Figure 4.2**, a single peak for heat release during the curing reaction extends approximately from 140 to 180 °C. The curve shifts slightly with the heating rate; for example, reducing the heating rate to 5 °C/min will move the peak to the left by about 5 °C. Meanwhile, this temperature range is also very close to literature values.[53] Therefore, we take 140-180 °C

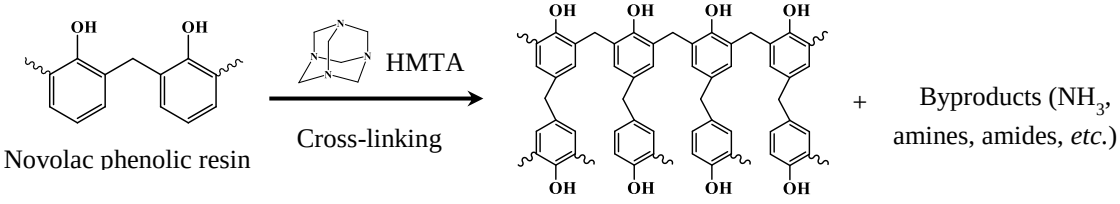

Figure 4.1. Schematic illustration of the curing reaction between phenolic resin and HMTA.

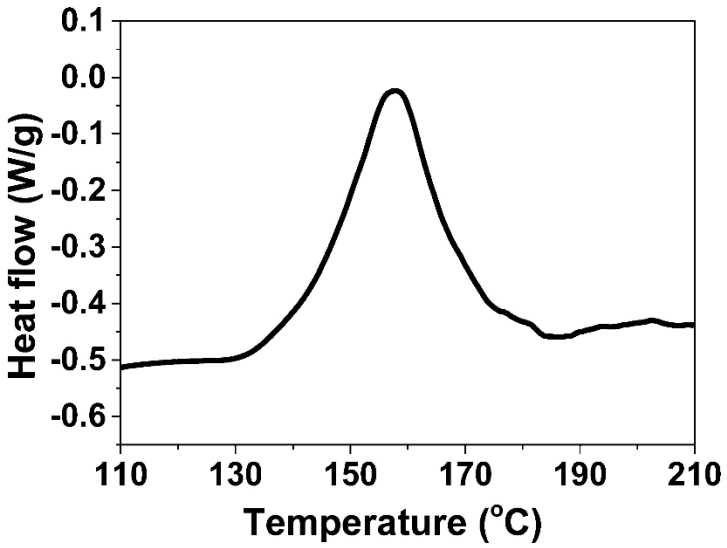

Figure 4.2. Dynamic DSC curve of an HMTA/resin mixture at a heating rate of 10 °C/min.

as the approximate temperature range of the curing reaction when selecting our coating temperatures.

4.2 Resin Coating Process

The underlying physical and chemical processes are depicted in **Figure 4.3**. After resin is added into the vessel, it is melted by the high temperature and is thus able to flow and mix with the preheated particles. High-speed stirring facilitates the distribution of the melt resin over the particle surface as well as among different particles. It induces fast shear motion between particles, which evens the melt distribution and prevents particle aggregation. As soon as the HMTA solution is added and makes contact with the particles, water quickly evaporates under the high temperature. Although HMTA can be dispersed among particles by mechanical stirring, molecular diffusion within the coating layers is still needed for a uniform cross-linking density. As cross-links are formed, the resin becomes increasingly

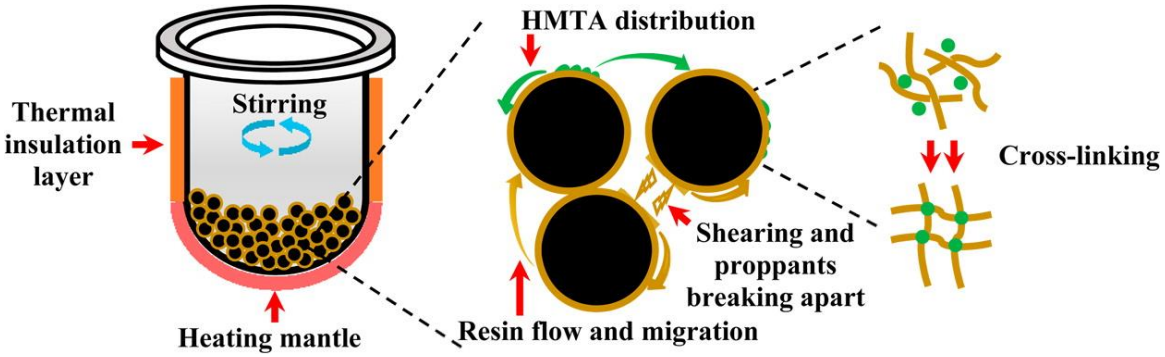

Figure 4.3. Schematic illustration of the coating process.

viscous and eventually solidifies with the formation of the polymer network, which not only freezes the resin flow but also drastically slows down the HMTA diffusion. In addition, if the cross-linking rate is faster than the dynamic contact between particle surfaces, bonds will be formed bridging the coating layers of different particles, resulting in particle agglomerates. Other processes such as heat-induced coating damages may also occur due to the high processing temperature. These simultaneous processes, including the redistribution and diffusion of HMTA, curing reaction, particle collision and breakup, and heat-induced coating damages, compete with one other and the coating outcome is determined by their dynamic and complex coupling. How to control the operating parameters for an optimized competition profile of these processes, or best coating outcome, is the central challenge of the study.

4.3 TGA Investigation

TGA tests were performed on the coated proppants to determine the amount of resin successfully applied onto the proppant surface. TGA curves for two coated samples, with

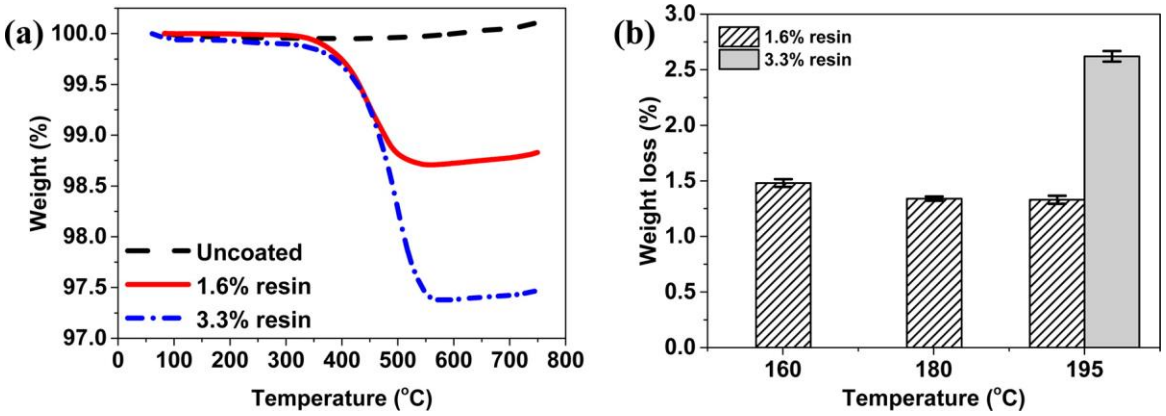

Figure 4.4. (a) TGA curves for uncoated and coated proppants with different resin-to-proppant ratios and (b) percentage weight loss of coated particles in TGA for different conditions.

resin-to-proppant ratios of 1.6% and 3.3% (hereinafter, resin-to-proppant ratios are measured by the weight ratio between the amount of resin added and the amount of proppants to be coated) and prepared with a CT process at T = 195 °C, are shown in **Figure 4.4a** along with that of uncoated proppants. Resin decomposition mostly occurs in the range of 350-550 °C and the total weight loss reflects the weight of resin coatings. The percentage weight loss after TGA, measured by the ratio of weight loss to the weight of uncoated proppant substrates, is plotted in **Figure 4.4b** (three different temperatures for the resin-to-proppant ratio of 1.6% and 195 °C for 3.3%). In all cases, the weight of resin coatings is only slightly lower than the total amount of resin initially added, and there is no substantial dependence on variations in process conditions. This observation is also valid for other coating conditions not shown here. As such we are confident that most resin has been successfully coated and retained on the proppant surface and for the same resin-to-proppant ratio, the amount of resin coatings is similar for different process conditions.

4.4 Effects of Resin Dosage

The effects of resin dosage on coating properties were investigated for two resin-to-proppant weight ratios (1.6% and 3.3%), and they are shown in **Figure 4.5**. Compared with the uncoated proppants (0%), improvements brought by the resin coating layer are dramatic: there is a 4-fold reduction in acid solubility for both resin-to-proppant ratios and crush weight loss is cut by more than half at least in the higher resin-to-proppant ratio case. The success of resin coatings in improving proppant performance is thus evident. The cured resin layer makes it more difficult for the acid molecules to penetrate and erode the particles. The crush protection function of the resin coating is multifold. In addition to the direct enhancement of the mechanical strength of proppants, the coating can also encapsulate the fines in the event of proppant crushing and thus maintain the structural integrity of the grain.[5] Furthermore, even for the ruptured particles, the resin can still act as a glue that holds the fines together in larger pieces. This last effect is clearly seen by comparing the

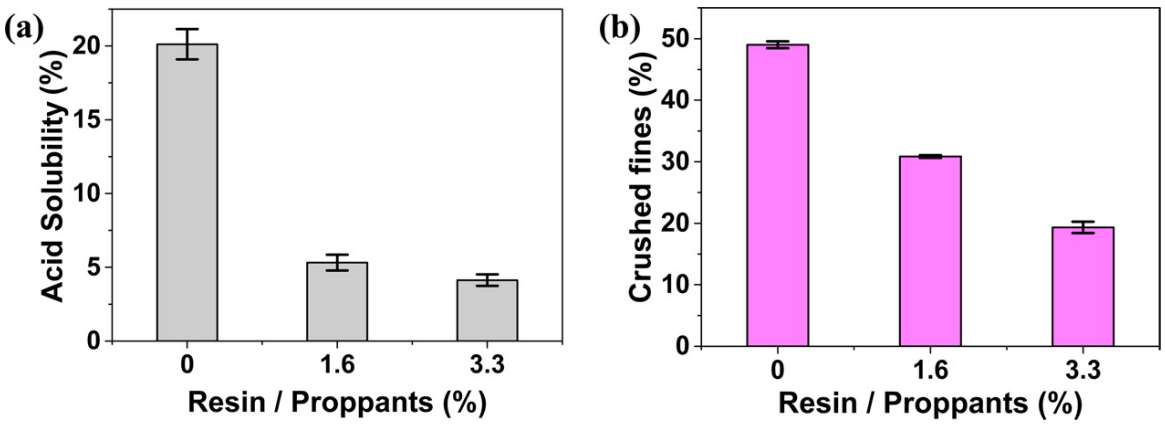

Figure 4.5. Influence of the resin-to-proppant ratio on the acid solubility and crush resistance of the coated proppants prepared by the CT process at 195 °C.

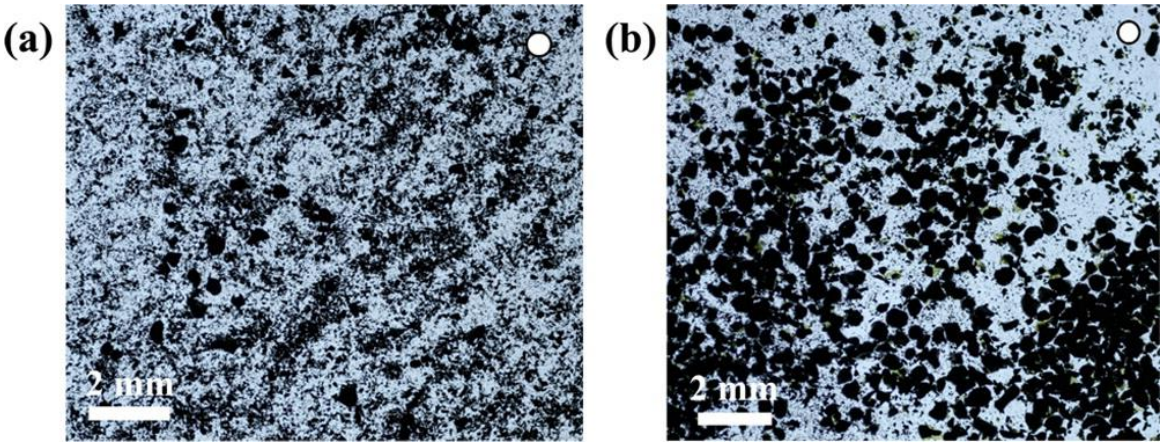

Figure 4.6. Images of the crushed fines from (a) uncoated proppants and (b) resin-coated proppants. White circles at the top-right corner show a typical proppant size of 0.6 mm.

photographs of the crushed fines (which passed through a 40-mesh sieve) from uncoated and coated proppants with 1.6% resin, as shown in **Figure 4.6**. Smaller fines were observed for the uncoated proppant compared to the resin-coated proppant.

The marginal benefit of increasing the resin-to-proppant ratio from 1.6% to 3.3% is noticeable but limited: the percentage weight loss in the crush test is reduced by a further 10%, but improvement in acid resistance is not significant. A larger amount of resin on the proppant surface increases the coating thickness and strength, thereby providing better tolerance to high pressure, whereas a thin layer of cured resin seems to be sufficient for acid protection. Since resin usage is a major contributor to the overall cost of the process, we focus the rest of the study on optimizing the coating performance with less resin (i.e., resin-to-proppant ratio of 1.6%) but by changing the coating process parameters. With the cost of phenolic resin estimated at ~2 U.S. dollars per kg, this dosage is going to increase the manufacturing cost by ~32 U.S. dollars per tonne of uncoated proppants.

4.5 Effects of Process Temperature Profile

4.5.1 Constant Temperature (CT) Process

We started by holding the temperature constant for the entire process (**Figure 3.1a**) and tested several different temperature levels. SEM images of these samples are shown in **Figure 4.7**. From the surface images (**Figures 4.7a-4.7d**), it is clear that a constant high process temperature (e.g., 195 °C) results in a rough surface (with more bumps), while a comparatively low temperature (e.g., 150 °C) gives better surface smoothness. The cross-sectional images in **Figures 4.7e-4.7h** were taken from manually crushed proppant particles, in which consistent coated layers of about 3-6 nm are clearly visible. We have also tested the effects of the HMTA addition method and found that the surface morphology of the

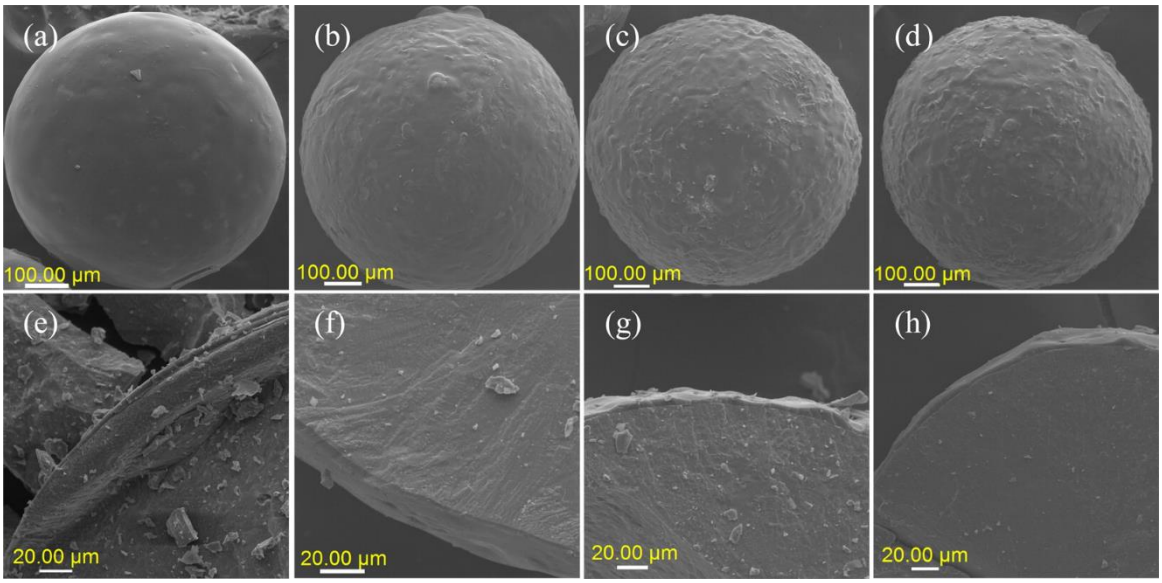

Figure 4.7. SEM images of the resin-coated proppants and their cross-sectional images prepared by the CT process at (a) and (e) 150 °C, (b) and (f) 160 °C, (c) and (g) 180 °C, and (d) and (h) 195 °C.

obtained coating layer is indistinguishable whether the HMTA solution was added as droplets or as a fine mist. Although spraying gives a more uniform macroscopic distribution among particles, as discussed below, it is the mixing at the molecular level, which relies on diffusion, that determines the surface quality.

When drips of HMTA solution hit the resin surface, local spots with high HMTA concentration are formed. At high temperature the high reaction rate quickly leads to the gelation of these spots before HMTA is dispersed to broader regions, while the adjacent resin remains at the melt state. Limited mobility and slower diffusion in these gel spots keep HMTA distribution localized, whereas the surrounding resin melt can still flow inward to react with HMTA and further strengthen the gelled regions, thereby amplifying the surface inhomogeneity. Meanwhile, a low temperature has a lower reaction rate, thereby allowing more time for HMTA molecules to diffuse across the coating layer and migrate to different particles. Even distribution of the cross-linking agent ensures that the reaction proceeds uniformly across all regions. Since resin flow and HMTA distribution are able to reach a dynamic equilibrium faster than the curing reaction, the whole resin layers reaches the gel point at about the same time, leading to a smooth and homogeneous surface morphology.

For resin coating layers with the same microscopic coating quality, a uniform cured resin coating surface with few flaws should provide superior acid solubility and crush resistance properties than an inhomogeneous one. Flaws, such as regions with limited resin (thinner

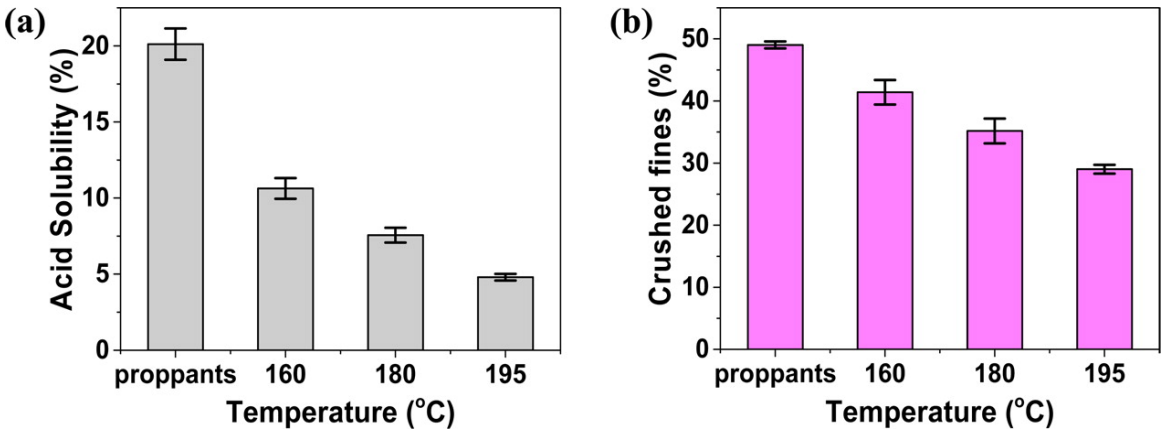

Figure 4.8. Acid solubility and crush resistance of the uncoated and resin-coated proppants prepared by the CT process at 160, 180, and 195 °C.

coating), may encourage preferential acid attack in the acid solubility test and which may act as stress points resulting in failure in the crush resistance test.

This prediction is however opposite to the coating performance results shown in **Figure 4.8**, where both acid and crush resistances improve with the temperature despite the worsening surface morphology. It is thus clear that the microscopic structure of the coating layer has also changed with the process temperature. Indeed, as seen from our DSC analysis in **Figure 4.2**, the curing reaction occurs over the range of approximately 140 to 180 °C. A temperature as low as 150 or 160 °C is likely not sufficient for all cross-linking bonds to be formed, leading to lower cross-linking density. The resulting coating layers are likely more porous, permeable to acid molecules, and susceptible to mechanical damage. For the lowest process temperature tested (150 °C; not shown here), we have also extended the final holding temperature from 3 to 20 min. Coating performance does not improve with the longer holding time, confirming that our current retention time is sufficient for highest

coating quality at the temperature (the coating actually deteriorates with prolonged heating, which we will discuss below). Meanwhile, at a high process temperature of 195 °C, cross-linking density is close to its maximum. Improved microscopic density at higher temperatures overcomes the nonuniformity in the film thickness, yielding a cured resin with improved acid resistance performance and mechanical strength. This opposite temperature dependence between surface smoothness and coating performance prompted us to further explore the temperature profile for an optimized coating outcome.

4.5.2 Ramping Temperature (RT) Process

As discussed in Section 3.2, the hot-melt coating method involves complex coupling between multiple physical and chemical processes. Many of them, including the reaction kinetics, HMTA diffusion, and resin rheology, depend strongly on temperature. Adjusting the temperature profile of the process is thus the most delicate yet most powerful means for the control and optimization of the coating process. For the CT process discussed above, lower temperature gives smooth coating surface, whereas higher temperature is required to complete the cross-linking reaction. We thus tested a new process (**Figure 3.1b**) where the temperature starts low to avoid fast initial gelation and allow sufficient time for the molecular mixing of HMTA in the resin layer. After a smooth surface is formed and partially cured, the temperature is gradually ramped up to bring the curing reaction to completion for a high final cross-linking density. The initial temperature we chose is 145 °C, which is close to the lower end of the range identified from DSC (**Figure 4.2**), and different final temperatures (175 and 195 °C) were tested. These two temperature profiles will be

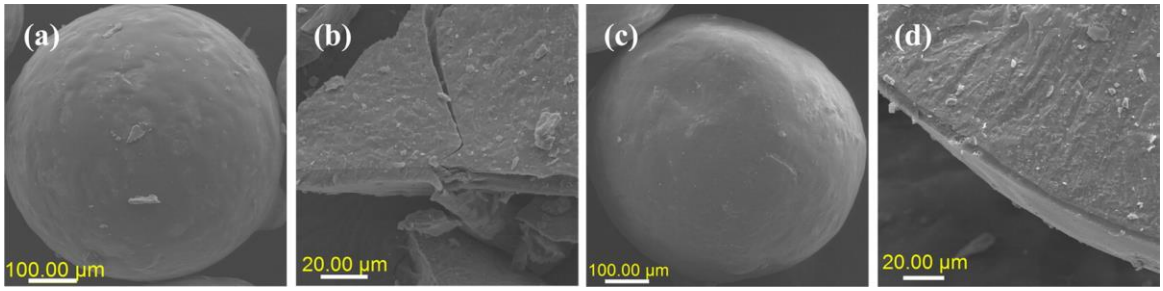

Figure 4.9. SEM images of resin-coated proppants and their cross sections prepared by the RT process with the initial/final temperatures of (a) and (b) 145/175 °C and (c) and (d) 145/195 °C.

denoted by 145/175 °C and 145/195 °C, respectively. **Figure 4.9** shows the SEM images of resin-coated particles prepared using this ramping temperature process. The cured resin surface morphology for both cases, shown in **Figure 4.9a** and **4.9c**, appeared smooth and homogeneous and were comparable to the surface morphology obtained from the CT process at a low temperature of 150 °C (**Figure 4.7a**). Cross-sectional images in **Figure 4.9b and 4.9d** indicated uniform cured resin layers of about 6 nm.

Figure 4.10 shows the properties of resin-coated proppants prepared by the RT process with final temperatures of 175 and 195 °C, compared with those of the CT process at 195 °C. It is clear that higher final temperature results in better acid and crush resistance of the coated particles, which can be attributed to the higher cross-linking degree of the coating layer. This is also consistent with the trend observed in the CT process described above. However, comparing the results of the 145/195 and 195 °C cases, it is interesting to see that the coated proppants prepared at a constant temperature of 195 °C exhibit slightly better overall performance despite its inferior surface quality. Specifically, its acid resistance is noticeably better than that of the RT process, whereas for the crush test, results

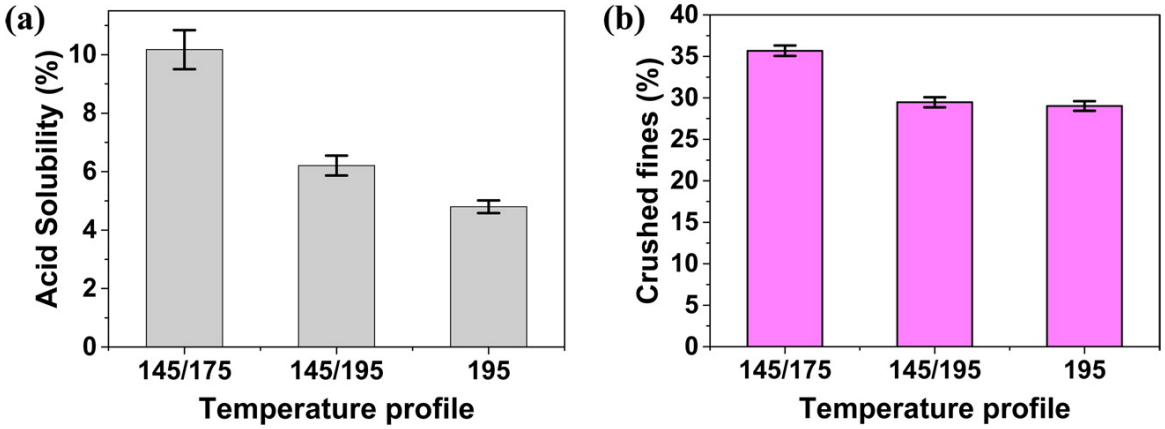

Figure 4.10. Properties of resin-coated proppants prepared by the RT process with the initial/final temperature of 145/175 °C and 145/195 °C, compared with the CT process case at 195 °C.

from the two processes are at the same level. Considering that the coating layer from the RT process is clearly more uniform and smoother and a final temperature of 195 °C should ensure a similar conversion as the CT process (at the same temperature), it is expected that the outcome of the RT process should be at least at the same level of the CT one. However, one factor that has not yet been considered is the difference in the retention time between the two processes (see **Figure 3.2**): the RT process (145/195 °C) takes about 20 min after curing is initiated whereas for the CT process (195 °C) it is only about 3.5 min. Longer time is needed in the former case to raise the temperature across the vessel. As discussed above, film thickness and microscopic structures are the two major factors determining coating performance. Despite the more uniform thickness, prolonged heating in the RT process may damage the latter and lead to deterioration in coating performance.

To test this hypothesis, different processing durations were tested. Using the CT process at 180 °C, HMTA was added to the reactor to initiate curing, which generally took ~1 min

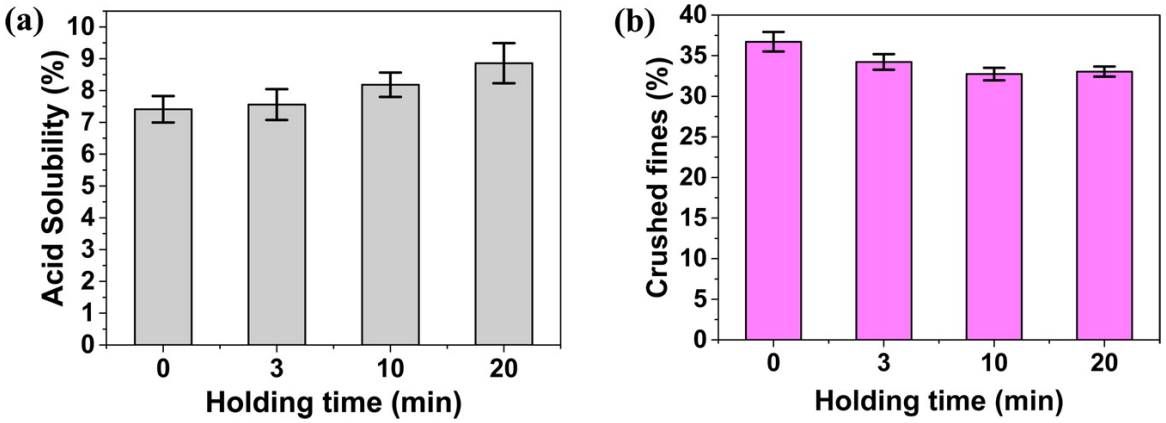

Figure 4.11. Effects of the final holding time on the performance of resin-coated proppants prepared by the CT process at 180 °C.

(curing was signified by resin-coated proppants breaking apart and no longer sticking to each other). We then varied the duration that the resin-coated proppants were held in the reactor before discharging, that is, the additional time for heating and stirring after proppant break-apart (defined as holding time, the standard choice so far is 3 min). Holding times of 0, 3, 10, and 20 min were investigated. The performance of the resulting resin-coated proppant was shown in **Figure 4.11**. Acid resistance (**Figure 4.11a**) clearly deteriorates with heating time and the effect becomes obvious for a holding time of 10 min: note that this is still shorter than the heating time in the RT process. Worsening acid resistance indicates a more porous microscopic structure in the resin, likely as a result of chemical bond breakages caused by the prolonged heating. Impact on the crush resistance is more subtle (**Figure 4.11b**): there seems to be a slight initial decrease (between 0 to 3 min) in crush weight loss but the measurement soon plateaus. Results from this test are consistent with observations in **Figure 4.10** where the RT process leads to slightly worse acid resistance but its crush test result is comparable with the CT process. It thus confirms the

impact of total heating time on the coating performance. Since how fast we can ramp up the temperature is eventually limited by the heat transfer rate of the setup, this limitation is inevitable for the RT process and will only get worse when the process is scaled up. As such, we conclude that as far as proppant performance is concerned, a CT process with high temperature (195 °C) is optimal. The RT process only becomes a viable option when surface morphology is an important consideration.

4.6 Effects of Particle Shape

Having complete surface coverage is a prerequisite for coating-layer effectiveness. Flaws, such as regions not sufficiently covered by resin or those where the resin is not cured, undermine the proppant performance. Spherical particles are more likely to receive a full coverage of uniform coatings for their symmetry. Irregularly shaped particles, on the other hand, are more prone to coating defects and nonuniformity, owing to the difficulty of achieving even resin/HMTA distribution thereon. Proppants are often commercially

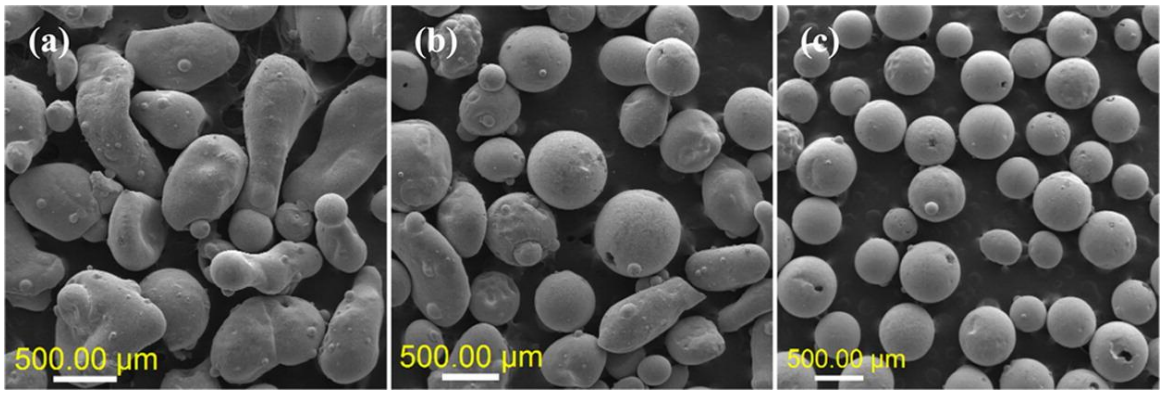

Figure 4.12. SEM images of the proppants with different shapes: (a) irregular, (b) as-received, and (c) spherical.

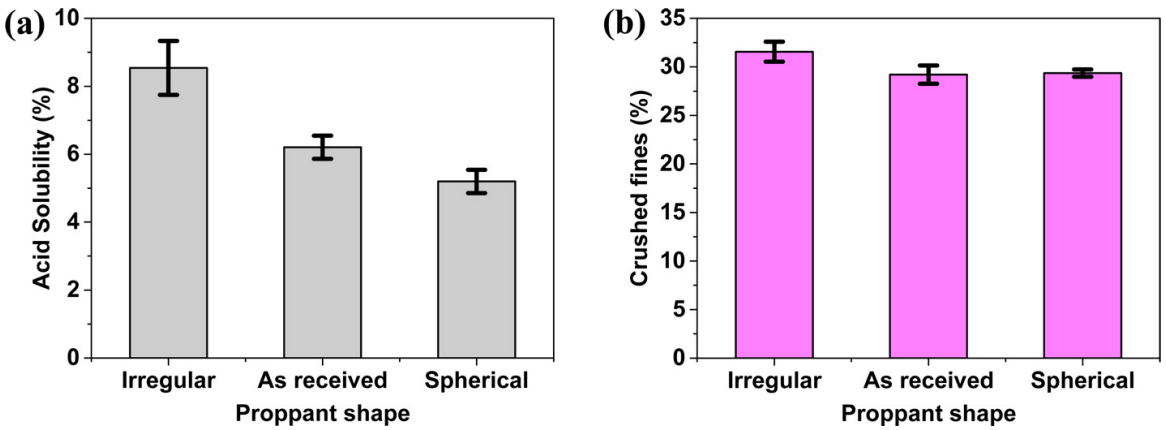

Figure 4.13. Performance of resin-coated proppants of different shapes (prepared by the RT process with the initial/final temperature of 145/195 °C).

available as mixtures of particles with assorted shapes. To weigh the improvement of selecting spherical proppants for coating against its additional cost, we use a spiral separator to sort out the spherical proppants from irregular ones. SEM images of the proppants with these different shapes are shown in **Figure 4.12**. Resin coatings were applied by the RT process with a final temperature of 195 °C. Coating performance of these samples are compared with one another and shown along with that of as-received proppants in **Figure 4.13**. Interestingly, the resin-coated spherical proppants show significantly better acid resistance while no noticeable change is observed in the crush resistance result. This suggests that even for irregular proppants the surface coverage and coating strength are sufficient for all three cases to provide crush protection. Differences in coating quality for the three particle geometries are likely in the surface uniformity, quantity of defects and cross-linking density, to which the acid solubility result is more sensitive.

Chapter 5

Conclusions of Part I

Improving particle performance via polymer coatings is of interest to the oil and gas industry as well as many other industries. In this study, solid particles (proppants) were coated with novolac phenolic resin using a hot-melt coating process, and the resin was subsequently cured *in situ* to form a cross-linked coating layer. Resin coatings significantly improved the performance of proppants in terms of their resistance to acid attack, measured using an acid solubility test, and high-pressure crushing, measured using a crush resistance test. Challenges in developing a coating process that provides optimal proppant performance stem from the complex coupling between its multiple underlying physical and chemical processes, including the flow of resin melt, distribution and diffusion of HMTA, resin/HMTA curing reaction, particle aggregation and breaking apart, as well as heat-induced damages to the resin structure. A delicate balance between these processes is required for an optimal coating outcome. Temperature plays a central role in controlling these processes. Different process temperature profiles, including those with constant and ramping temperatures, were explored. In the case of resin coating and curing at constant temperature, lower constant temperatures were found to be more favorable for smooth surface morphology, whereas higher temperatures were needed for a strong and impermeable layer (even though more resin coating-layer defects may be present). This

dilemma reflects the complex dynamics between the curing kinetics and the mass transfer process: lower temperatures slow down the curing reaction and allow sufficient time for the uniform distribution of the cross-linking agent into the resin coating layer, whereas higher temperatures are needed to reach high conversion and cross-linking density. This conflict can be reconciled by a controlled temperature ramp, from which excellent surface quality is achieved without significantly sacrificing the coating performance. The coating performance itself, measured by acid and crush tests, is, however, not improved compared with the constant temperature process. This is due to the longer retention time of the process, which subjects the resin to prolonged exposure to heat and causes damages in its microscopic structure. Since the duration required for the temperature ramp is eventually limited by the rate of heat transfer from the reactor heating jacket to the reactor and its contents, it is concluded that a constant high temperature is still preferred for optimal coating performance in terms of acid solubility and crush resistance performance. Resin coating using ramping temperature is applicable when surface morphology is of concern. This study not only provides an efficient and scalable proppant-coating process optimized for application in hydraulic fracturing operations, the strategy demonstrated here is also generalizable to particle coating processes in many other industries.

Chapter 6

Future Work

In this study, a low-cost and efficient hot-melt coating process for solid particles is developed and two coating strategies are proposed (i.e., CT and RT processes). However, the applications of these coating methods are currently only limited to a laboratory scale. To enable practical applications in industry, further scale-up experiments much follow to ensure viability of the methods and detect any technical limitations they may have. We already observed that the rate of heat transfer is a concern when employing the RT process, and a long heating time is harmful to the coating performance. This limitation can get worse as the production setup scales up. How to minimize the impact of the heat transfer limitation without deteriorating the overall coating performance is one of the key issues that needs to be solved before using the RT coating process.

Another extension to consider is how to further improve the coating outcome while minimizing the usage of resins. We have shown that the CT process can lead to an optimal coating performance when a high temperature (i.e., 195 °C) is used, while the RT process should be used when a smooth surface morphology is required. Each process has an individual advantage which is not available in the other one. Therefore, a combination of these two processes can be an interesting issue to explore. For example, instead of introducing a single coating layer onto the solid particles via only one of the processes, one

can also develop double coating layers in which the first layer is realized via the CT process and the second one via the RT process. As a result, while the first coating layer provides primary resistance to acid erosion and high-pressure crushing, the second layer enables a homogeneous surface morphology of the resin-coated particles. Other variables such as the chemistry of resins for coating purpose and the usage of additives (e.g., fibre for reinforcement purpose) also worth further considerations when developing resin-coated particles with maximized coating performance.

Bibliography

(1) Goldschmidt, A.; Streitberger, H.-J. *BASF handbook on basics of coating technology*; Vincentz Network: Hannover, 2007.

(2) Wicks Jr, Z. W.; Jones, F. N.; Pappas, S. P.; Wicks, D. A. *Organic coatings: science and technology*; John Wiley & Sons: Hoboken, 2007.

(3) Donaldson, E. C.; Alam, W.; Begum, N. *Hydraulic Fracturing Explained: Evaluation, Implementation, and Challenges*; Gulf Publishing: Houston, 2013.

(4) Fink, J. *Hydraulic Fracturing Chemicals and Fluids Technology*; Gulf Professional Publishing: Waltham, 2013.

(5) Zoveidavianpoor, M.; Gharibi, A. Application of polymers for coating of proppant in hydraulic fracturing of subterraneous formations: A comprehensive review. *Journal of Natural Gas Science and Engineering* **2015**, *24*, 197.

(6) Zhang, K. Resin coated proppant slurry compositions and methods of making and using same. US Patent No. 20100256024, 2008.

(7) Nelson, E. B.; Brown, J. E.; Card, R. J. Sand control without requiring a gravel pack screen. US Patent No. 5551514, 1996.

(8) McLennan, J.; Walton, I.; Moore, J.; Brinton, D.; Lund, J. Proppant backflow: Mechanical and flow considerations. *Geothermics* **2015**, *57*, 224.

(9) Liang, F.; Sayed, M.; Al-Muntasheri, G. A.; Chang, F. F.; Li, L. A comprehensive review on proppant technologies. *Petroleum* **2016**, *2*, 26.

(10) Pangilinan, K. D.; Al Christopher, C.; Advincula, R. C. Polymers for proppants used in hydraulic fracturing. *Journal of Petroleum Science and Engineering* **2016**, *145*, 154.

(11) Naderhoff, B.; Toman, A. Resin coated particulates. US Patent No. 20110160101, 2010.

(12) Lecomte, F.; Siepmann, J.; Walther, M.; MacRae, R. J.; Bodmeier, R. pH-sensitive polymer blends used as coating materials to control drug release from spherical beads: importance of the type of core. *Biomacromolecules* **2005**, *6*, 2074.

(13) Sun, Y.-M.; Chang, C.-C.; Huang, W.-F.; Liang, H.-C. Fluidized-bed spray coated porous hydrogel beads for sustained release of diclofenac sodium. *Journal of Controlled Release* **1997**, *47*, 247.

(14) Karches, M.; Morstein, M.; Von Rohr, P. R.; Pozzo, R. L.; Giombi, J. L.; Baltanás, M. A. Plasma-CVD-coated glass beads as photocatalyst for water decontamination. *Catalysis Today* **2002**, *72*, 267.

(15) Swayampakula, K.; Boddu, V. M.; Nadavala, S. K.; Abburi, K. Competitive adsorption of Cu (II), Co (II) and Ni (II) from their binary and tertiary aqueous solutions using chitosan-coated perlite beads as biosorbent. *Journal of Hazardous Materials* **2009**, *170*, 680.

(16) Hasan, S.; Krishnaiah, A.; Ghosh, T. K.; Viswanath, D. S.; Boddu, V. M.; Smith, E. D. Adsorption of divalent cadmium (Cd (II)) from aqueous solutions onto chitosan-coated perlite beads. *Industrial & Engineering Chemistry Research* **2006**, *45*, 5066.

(17) Martin, C.; Ramirez, L.; Cuellar, J. Stainless steel microbeads coated with sulfonated polystyrene-co-divinylbenzene. *Surface and Coatings Technology* **2003**, *165*, 58.

(18) Tracton, A. A. *Coatings technology handbook*; CRC press: Boca Raton, 2005.

(19) Song, J.; Batra, A.; Rego, J. M.; Macosko, C. W. Polyethylene/polyurethane blends for improved paint adhesion. *Progress in Organic Coatings* **2011**, *72*, 492.

(20) O'Connor, A. E.; Macosko, C. W. Melt versus solvent coating: Structure and properties of block-copolymer-based pressure-sensitive adhesives. *Journal of Applied Polymer Science* **2002**, *86*, 3355.

(21) Patcas, F. C.; Garrido, G. I.; Kraushaar-Czarnetzki, B. CO oxidation over structured carriers: A comparison of ceramic foams, honeycombs and beads. *Chemical Engineering Science* **2007**, *62*, 3984.

(22) Balkus, K. J.; Scott, A. S. Molecular sieve coatings on spherical substrates via pulsed laser deposition. *Microporous and Mesoporous Materials* **2000**, *34*, 31.

(23) Balkus, K. J.; Scott, A. S. Zeolite coatings on three-dimensional objects via laser ablation. *Chemistry of Materials* **1999**, *11*, 189.

(24) Turton, R.; Cheng, X. X. The scale-up of spray coating processes for granular solids and tablets. *Powder Technology* **2005**, *150*, 78.

(25) Wesdyk, R.; Joshi, Y.; Jain, N.; Morris, K.; Newman, A. The effect of size and mass on the film thickness of beads coated in fluidized bed equipment. *International Journal of Pharmaceutics* **1990**, *65*, 69.

(26) Weiss, K. D. Paint and coatings: a mature industry in transition. *Progress in Polymer Science* **1997**, *22*, 203.

(27) Bauer, F.; Decker, U.; Dierdorf, A.; Ernst, H.; Heller, R.; Liebe, H.; Mehnert, R. Preparation of moisture curable polysilazane coatings: Part I. Elucidation of low temperature curing kinetics by FT-IR spectroscopy. *Progress in Organic Coatings* **2005**, *53*, 183.

(28) Licari, J. J. *Coating Materials for Electronic Applications: Polymers, Processing, Reliability, Testing*; William Andrew: Norwich, 2003.

(29) Chattopadhyay, D. K.; Raju, K. V. S. N. Structural engineering of polyurethane coatings for high performance applications. *Progress in Polymer Science* **2007**, *32*, 352.

(30) Ferrero, F.; Periolatto, M.; Udrescu, C. Water and oil-repellent coatings of perfluoro-polyacrylate resins on cotton fibers: UV curing in comparison with thermal polymerization. *Fibers and Polymers* **2012**, *13*, 191.

(31) Nikkola, J.; Mahlberg, R.; Mannila, J.; Jämsä, S. Effect of curing process on simulated antisoiling properties of sol–gel coating on pine sapwood. *Journal of Coatings Technology and Research* **2010**, *7*, 441.

(32) Chico, B.; Galván, J.; De La Fuente, D.; Morcillo, M. Electrochemical impedance spectroscopy study of the effect of curing time on the early barrier properties of silane systems applied on steel substrates. *Progress in Organic Coatings* **2007**, *60*, 45.

(33) Wang, X.; Li, G.; Li, A.; Zhang, Z. Influence of thermal curing on the fabrication and properties of thin organosilane films coated on low carbon steel substrates. *Journal of Materials Processing Technology* **2007**, *186*, 259.

(34) Fernandes, B. S.; da Silva Souza, K. G.; Aoki, I. V.; de Melo, H. G.; Amado, F. D. R. Evaluation of the influence of experimental parameters in the formation of a vinyltrimethoxysilane film on 1010 carbon steel through electrochemical impedance spectroscopy and contact angle techniques. *Electrochimica Acta* **2014**, *124*, 137.

(35) Lee, S. S.; Han, H. Z.; Hilborn, J. G.; Månson, J.-A. E. Surface structure build-up in thermosetting powder coatings during curing. *Progress in Organic Coatings* **1999**, *36*, 79.

(36) Barletta, M.; Lusvarghi, L.; Mantini, F. P.; Rubino, G. Epoxy-based thermosetting powder coatings: surface appearance, scratch adhesion and wear resistance. *Surface and Coatings Technology* **2007**, *201*, 7479.

(37) Yang, L.; Feng, J.; Zhang, W.; Qu, J.-e. Film forming kinetics and reaction mechanism of γ-glycidoxypropyltrimethoxysilane on low carbon steel surfaces. *Applied Surface Science* **2010**, *256*, 6787.

(38) Wang, Y.; Lieberman, M. Growth of ultrasmooth octadecyltrichlorosilane self-assembled monolayers on SiO2. *Langmuir* **2003**, *19*, 1159.

(39) Vallant, T.; Brunner, H.; Mayer, U.; Hoffmann, H.; Leitner, T.; Resch, R.; Friedbacher, G. Formation of self-assembled octadecylsiloxane monolayers on

mica and silicon surfaces studied by atomic force microscopy and infrared spectroscopy. *Journal of Physical Chemistry B* **1998**, *102*, 7190.

(40) Graham, J. W.; Sinclair, A. R. High strength particulates. US Patent No. 4585064, 1986.

(41) Johnson, C. K.; Armbruster, D. R. Particles covered with a cured infusible thermoset film and process for their production. US Patent No. 4439489, 1984.

(42) Sinclair, A. R.; Richard, L. J. I. Composite and reinforced coatings on proppants and particles. US Patent No. 5597784, 1997.

(43) Armbruster, D. R. Precured coated particulate material. US Patent No. 4694905, 1987.

(44) Dewprashad, B. Method of producing coated proppants compatible with oxidizing gel breakers. US Patent No. 5420174, 1995.

(45) Murphey, J. R.; Totty, K. D. Continuously forming and transporting consolidatable resin coated particulate materials in aqueous gels. US Patent No. 4829100, 1989.

(46) American Petroleum Institute (API) *API RP 19C: Measurement of Properties of Proppants Used in Hydraulic Fracturing and Gravel-packing Operations*; API: Washington, DC, 2008.

(47) Sangaj, N. S.; Malshe, V. Permeability of polymers in protective organic coatings. *Progress in Organic Coatings* **2004**, *50*, 28.

(48) Lin-Gibson, S.; Baranauskas, V.; Riffle, J.; Sorathia, U. Cresol novolac-epoxy networks: properties and processability. *Polymer* **2002**, *43*, 7389.

(49) Xiaoqing, Z.; Looney, M. G.; Solomon, D. H.; Whittaker, A. K. The chemistry of novolac resins: 3. 13C and 15N nmr studies of curing with hexamethylenetetramine. *Polymer* **1997**, *38*, 5835.

(50) Katovic, Z.; Stefanic, M. Intermolecular hydrogen bonding in novolacs. *Industrial & Engineering Chemistry Product Research and Development* **1985**, *24*, 179.

(51) Wang, X.-M.; Riedl, B.; Christiansen, A.; Geimer, R. Differential scanning calorimetry of the effects of temperature and humidity on phenol-formaldehyde resin cure. *Polymer* **1994**, *35*, 5685.

(52) Zhang, C.; Binienda, W. K.; Zeng, L.; Ye, X.; Chen, S. Kinetic study of the novolac resin curing process using model fitting and model-free methods. *Thermochimica Acta* **2011**, *523*, 63.

(53) De Medeiros, E. S.; Agnelli, J. A.; Joseph, K.; De Carvalho, L. H.; Mattoso, L. H. Curing behavior of a novolac-type phenolic resin analyzed by differential scanning calorimetry. *Journal of Applied Polymer Science* **2003**, *90*, 1678.

Part II

Molecular Dynamics Study of Polymer Networks

Chapter 7

Introduction

Network polymers are one of the most important classes of soft materials composed of multiple cross-linked polymer chains which assemble into a percolated three-dimensional structure.[1-3] The interconnections of molecular chains, either by permanent covalent bonds or non-covalent physical interactions, confers many unique properties to these materials, such as improved elasticity and modulus, and high resistance to heat and organic solvents.[4-6] Due to their superior performance, network polymers have been extensively employed in both of industrial practice and theoretical research. Typical examples are vulcanized rubber and cross-linked thermosetting polymers (e.g., epoxy resins and phenolic resins) which have been used for many years in the manufacture of automobile tires, apparel and coatings, *etc.*, and are still the focus in experimental and theoretical studies.[5, 7-9] In general, these materials can be synthesized by cross-linking of small molecules (i.e., monomers) or polymers with varying chain length. Both of these methods have been widely used based on the topology of chosen precursors. For instance, cross-linked phenolic resins can be synthesized from phenols and formaldehydes by controlling the molar ratio of the two monomers. While a similar product can be also prepared by curing novolac phenolic resins, which are long linear polymer chains, with a cross-linking agent. However, a fundamental understanding of the effects of precursor topology on the prepared polymer networks has

never been revealed in previous studies. Solving such an issue in real experiments may be non-trivial, due to the unpredictable complexity usually involved in polymerization reactions.

Recent development in computer power have made simulation technique a powerful tool to study polymer materials, in which molecular dynamics (MD) simulation and Monte Carlo (MC) simulation are two primary techniques used in most of computational studies in polymer fields.[10, 11] In these simulations, a simple coarse-grained bead-spring model has gained widespread usage in studying polymer melts and networks.[10, 12] Such model has been reported to be able to capture the essential characteristics of these polymer systems.[13] Comparing with experiments, computer simulations show an advantage in controlling the cross-linking process, and various approaches can be used to prepare molecular models of polymer networks, in which cross-linking procedures and precursor topologies are common variables to control. In early studies of Leung et al.[14, 15], polymer networks are generated using a strategy analogous to "solid-state" polymerization, in which the precursor molecules with realistic configurations are randomly placed into the simulation box but kept static in the subsequent polymerization process. Cross-linking reactions between the reactive groups are then performed based on a probabilistic algorithm with an increasing reaction radius. While allowing intra-molecular reactions to take place and thus their influence on the prepared networks can be investigated, this method however does not consider the mobility and possible entanglement effects of polymer chains. Duering et al.[16, 17] and Grest et al.[18] instead focused on a dynamic cross-linking process. In these studies, polymer networks were prepared by dynamically cross-linking the homopolymers with

multifunctional cross-linkers. Molecules are allowed to move around in a dynamic way, based on their interactions with other molecules. Cross-linking is triggered when the distance between a free chain end and unsaturated cross-linkers is within the chosen reaction radius. Kinetics of the cross-linking process then can be directly investigated by recording the time evolution of the reactants. Such a dynamic cross-linking process is also employed by many other MD studies.[19-21] Alternatively, Svaneborg et al.[22] and Rottach et al.[23, 24] used a random, instantaneous cross-linking strategy, in which a predetermined number of pairs of monomers within a chosen capture radius were randomly selected from the equilibrated polymer melts and cross-linked in a single step. In addition to these varying cross-linking procedures, precursor topology is another parameter which varies significantly among different studies. Precursors with various chain lengths have been used to prepare polymer networks. Duering et al.[17] studied the kinetics and relaxation of end-linked polymer melts with chain length ranging from 12 to 100. By using a cluster search algorithm, structure analysis of the resultant networks was performed, which allowed the authors to compare their prepared networks to the theoretical predictions of rubber elasticity. Sliozberg et al.[25] used long precursors with chains length of up to 246 to synthesize entangled polymer networks. The mechanical and viscoelastic properties of the prepared networks, with varying cross-linking degrees, are then correlated to their structures. Although various choices in cross-linking strategies and precursors have been used when preparing polymer networks, a fundamental understanding of the effects of the preparation methods on the formation, structure and properties of polymer networks is not available. These choices may actually have a significant impact on the prepared networks.

Indeed, in a work of Hosono et al.[21], rigidity of precursor chains was found to have a substantial influence on the homogeneity of synthesized networks, in which flexible precursor chains led to an inhomogeneous network structure on a large scale due to the formation of microgel clusters, whereas a homogeneous network could be obtained by using the rigid precursors. Effects of other factors, such as architecture of cross-linkers (e.g., functionality, symmetry and shape), on the polymer networks can be also seen in previous studies.[19, 26]

Meanwhile, MD technique have been widely used in the studies of polymer networks, as it provides a dynamic evolution of the system and is useful in studying the kinetics of network formation. However, most of the previous studies were focusing on the end-linking process. In this work, we use MD simulations to virtually synthesize polymer networks from three sets of precursors with varying chain length. Instead of applying the end-linking process which eventually results in essentially different network structures (e.g. averaged strand length, *etc.*) in our case, we enable cross-linking reactions to occur at multiple sites along the polymer chains by regularly placing reactive atoms on the backbone of precursors. The three precursors are designed in a way that ideally they would form an identical network after cross-linking process is complete. Our purpose is to investigate the effects of precursor topology on the formation, structure and properties of polymer networks. While providing insights into the structure-property relationship of cross-linked polymers, this study also can serve as a guidance in developing molecular model of polymer networks from different precursors.

Chapter 8

Methodology

8.1 Molecular Model and Precursor Systems

Three sets of systems were investigated, namely monomer-monomer (MM), long chain-monomer (LM) and short chain-short chain (SS) systems (**Figure 8.1**). The LM system is composed of long polymer chains (199 beads) and monomers, while all the molecules in the MM and SS systems are single monomers and short polymer chains (5 beads), respectively. The polymer chains are modeled as freely jointed bead-spring molecules[12], and the monomers are represented by single beads. The pair interaction between topologically unconnected particles is described by the standard truncated 12-6 Lennard-Jones (LJ) potential, given by

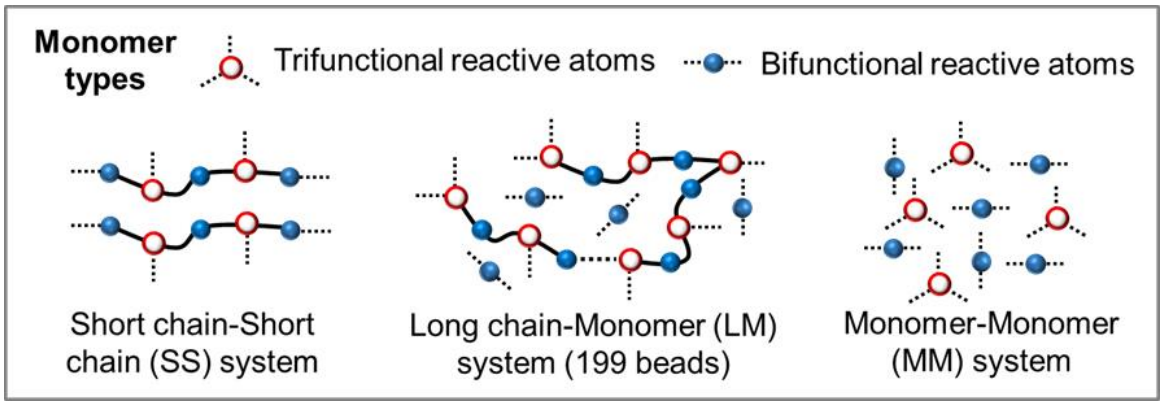

Figure 8.1. Topology of the three sets of precursors used to prepare polymer networks. Dashed lines indicate possible bonds each monomer can form.

$$U_{lj}(r) = \begin{cases} 4\varepsilon\left[\left(\frac{\sigma}{r}\right)^{12} - \left(\frac{\sigma}{r}\right)^{6}\right] + C & r < r_c \\ 0 & r \geq r_c \end{cases}$$

where r is the distance between the particles, r_c is the cut-off distance chosen at 2.5, and ε and σ are LJ units of energy and distance, respectively. A constant C is used to ensure that the LJ potential is continuous everywhere. For connected particles, an anharmonic interaction known as finite extension nonlinear elastic (FENE) potential is applied in addition to LJ interaction.

$$U_{FENE}(r) = \begin{cases} -\frac{1}{2}kR_0^2 \ln\left[1 - \left(\frac{r}{R_0}\right)^2\right] & r < R_0 \\ \infty & r \geq R_0 \end{cases}$$

Standard parameters are used for the maximum bond length $R_0 = 1.5\sigma$, at which the elastic energy of bond is infinite, and the spring constant $k = 30\varepsilon/\sigma^2$, which is small enough to allow using a relatively large time step while sufficiently large to prevent bonds from cutting through each other.[17] In the simulation, the equations of motion are integrated by velocity-Verlet algorithm with a time step $\Delta t = 0.005\tau$, where τ is LJ unit of time expressed by

$$\tau = \sigma\sqrt{\frac{m}{k_B T}}$$

where m is the unit mass, $T = \varepsilon/k_B$ is the temperature and k_B is the Boltzmann constant. Periodic boundary condition is applied in all studied processes, and simulations are carried out using Large-scale Atomic/Molecular Massively Parallel Simulator (LAMMPS) developed by Sandia National Laboratories.

8.2 Melt Equilibration and Network Preparation

The polymer chains and/or monomers are initially randomly placed into the simulation box with a number density of 0.85. The particles are allowed to overlap. To reduce finite size effects, 50000 monomers are used in all three systems. Two different methods, namely fast push-off[27] and Dissipative Particle Dynamics (DPD) push-off[28] algorithms, are employed to prepare a well-equilibrated melt. The procedures using these two methods for melt equilibration are briefly introduced as follows. More details can be found in the literatures.[27, 28]

Considering the small molecular weight of the monomers and short polymer chains, a fast push-off method is used for equilibration of MM and SS systems. In this method, a weak excluded volume interaction is introduced to separate the highly-overlapped monomers from each other. One of the soft potentials, named cosine potential, is often used for this purpose.

$$U_{soft}(r) = \begin{cases} A[1 + \cos(\frac{\pi r}{r_c})] & r < r_c \\ 0 & r \geq r_c \end{cases}$$

Where the cut-off distance is $r_c = 2^{1/6}\sigma$. In the fast push-off process, the initial amplitude A is increased from 4ε to 200ε over a short time interval of 10τ. The system is then switched to full LJ potential and equilibrated for a short MD run.

However, this fast push-off method is not feasible for the equilibration of long polymer chains, as it results in deformation of the polymers on short to intermediate length scales

during the push-off step.[27] Due to the slow reptation dynamics of long chains, it requires an extremely long MD run to fully relax the molecules. Therefore, a different equilibration protocol, known as DPD-push-off, is used to equilibrate the LM system. The method uses a different soft repulsion potential with a cut-off distance $r_c = \sigma$.

$$U_{DPD}(r) = \begin{cases} \frac{a_{DPD}}{2} r_c (1 - \frac{r}{r_c}) & r < r_c \\ 0 & r \geq r_c \end{cases}$$

Where maximum repulsion parameter a_{DPD} is selected at $25k_BT$ initially. The system is then simulated for 500τ before increasing the parameter a_{DPD} from $25k_BT$ to $1000k_BT$ over a time interval of 5.5τ. Finally, MD simulation with full LJ potential is performed for $10^4\tau$.

Polymer networks are prepared by cross-linking reactions among the reactive monomers after the precursor melts are fully equilibrated. In the simulations, the reactive monomers (bifunctional and trifunctional) are present in stoichiometric proportion. A new FENE bond is formed when the distance between two different reactive monomers is less than the critical reaction radius $d = 1.0\sigma$. Temperature is maintained at $T = 1.0\varepsilon/k_B$ during the cross-linking reactions, using a Nose-Hoover thermostat with a damping constant of 0.5τ.

8.3 Network Characterization

We utilize a so-called "structure searching method", as proposed by Duering et al.[29], to analyze the structure of the prepared polymer networks. Briefly, a burning method[30] is applied to remove all the monomers in the structural defects (e.g., dangling chains and

loops) within the largest cluster, resulting in a perfect network. Elastic strands and junctions in the network then can be identified and counted. In our trifunctional polymer network, a cross-linking junction is considered to be elastically active only when all three of its reactive sites are attached to the network, and elastic strands are those ended with two such elastic junctions. Other strands, such as dangling and free chains, are elastically inactive since only one end of these strands at most is connected with elastic junctions.

Glass transition temperatures (*Tg*) of the final polymer networks are measured by the changes in specific volume (i.e., volume per monomer) as the temperature decreases slowly. An isothermal-isobaric (*NPT*) ensemble is used during the simulations, with reduced pressure maintained at $P = 0.5$. The cooling rate is chosen at $0.8\varepsilon/k_B$ per million steps. Prior to the measurements, the polymer networks are subjected to alternate heating and cooling processes for a few cycles, in which the changing rate of temperature is maintained at the same value as the desired cooling rate, to avoid the effects of thermal history.

Elastic moduli of the polymer networks are measured by conducting tensile deformation simulations. In the test, the simulation box is deformed in both positive and negative z directions with a constant true strain rate of $\dot{e} = 0.0327/\tau$ which causes a change in the box dimension with time as

$$L(t) = L_0 \exp(\dot{e}\Delta t)$$

where L_0 is initial box length. The deformation simulations are performed under the *NPT* condition with pressure applied on another two dimensions (i.e., x and y directions) set at

0, allowing a dynamic response of the pressures to the tensile deformations. The tensile stress σ_{ts} and strain ϵ_{ts} are then calculated by

$$-\sigma_{ts} = P_z - \frac{1}{2}\left(P_x + P_y\right)$$

$$\epsilon_{ts} = \frac{L - L_0}{L_0}$$

where P_x, P_y and P_z are stresses at x, y and z directions, respectively, and L is the final box length in z direction.

Chapter 9

Results and Discussion

9.1 Network Formation and Structure

The final polymer network is chosen in a way that all three networks have a similar number of elastic strands (this parameter shows a strong correlation with network modulus, and will be discussed in more details later). As shown in the **Figure 9.1a**, degree of atom saturation, defined as number of bonds in network divided by total possible bonds (i.e., 60000), of the three networks has almost reached the maximum level (>98%). **Figure 9.1b** shows the evolution of the weight-averaged molecular weight (*Mw*) of the SS, LM and MM systems as the network formation processes proceed. As expected, a more rapid gelation,

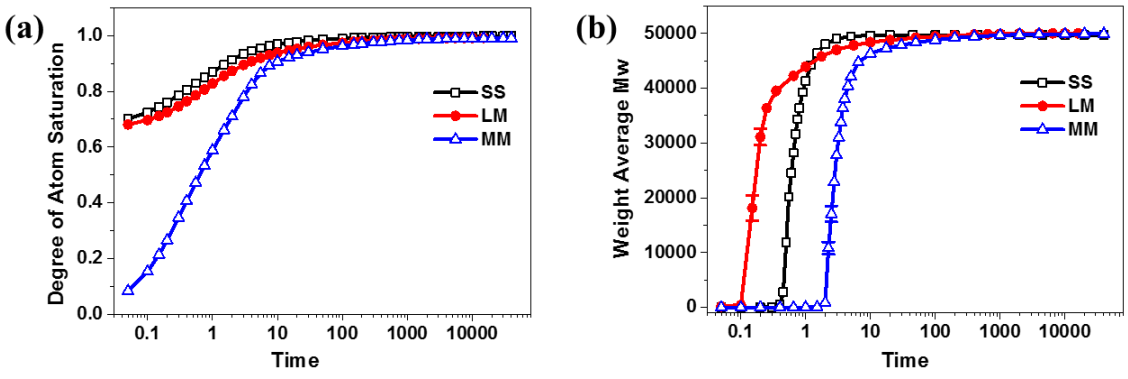

Figure 9.1. Temporal evolution of (a) degree of atom saturation and (b) weight-averaged molecular weight of SS, LM and MM systems. Error bars smaller than symbol size are not shown.

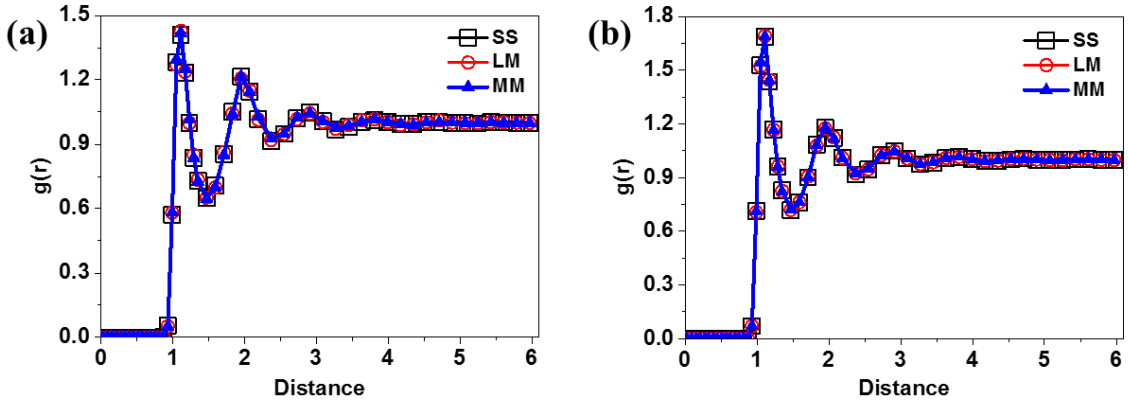

Figure 9.2. Radial distribution function of (a) all atoms in polymer networks and (b) bifunctional atoms using trifunctional atoms as reference.

which is indicated by a sharp increase in molecular weight, can be observed as the chain length of precursors increases. This phenomenon stems from the fact that in a system composed of longer polymer chains, lesser new bonds are needed to form a polymer network, resulting in a higher gelation rate. In final stages (e.g., > 200τ), the increase of *Mw* is insignificant and *Mw* of final networks are also close to the maximum (i.e., 50000).

Radial distribution function (RDF) is used to characterize the overall homogeneity of the final networks. RDF of the whole network using all beads in the system as reference particles and RDF of the bifunctional beads using trifunctional beads as reference are shown in **Figures 9.2a** and **9.2b**, respectively. No significant difference among the final networks is found in their local density variations.

By employing the "burning method", the network structure is analyzed in details. The results are summarized in **Table 9.1** and **Figure 9.3**. Most of dangling chains are actually dangling single beads. As shown in **Table 9.1**, the MM network has the largest number of

Table 9.1. Structural parameters of the final networks.

Systems	Number of dangling chains	Number of dangling atoms	Number of elastic junctions	Number of elastic strands
SS	547 ± 8	1067 ± 29	18705 ± 24	28057 ± 36
LM	606 ± 5	655 ± 6	18712 ± 4	28068 ± 5
MM	646 ± 18	1285 ± 41	18645 ± 19	27968 ± 29

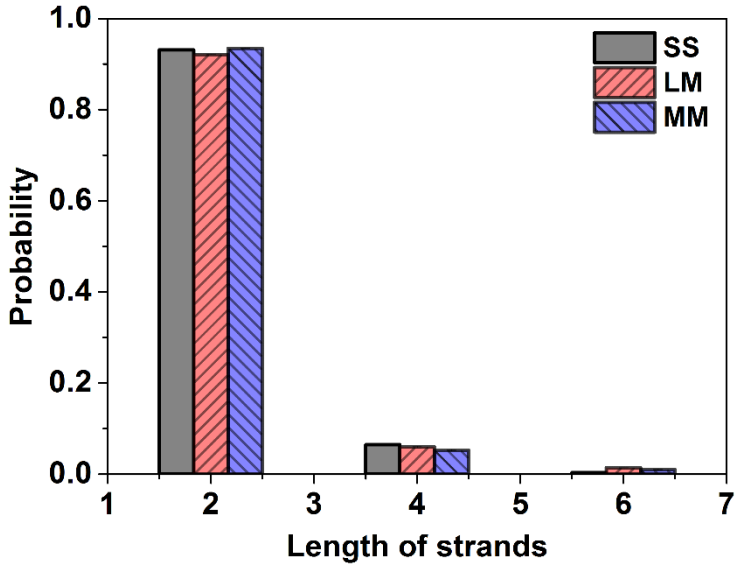

Figure 9.3. Statistical distribution of elastic strands measured by the number of consisting bonds. Error bars are not shown due to small values.

dangling chains while the SS network has the least, although the difference in this structural parameter is still limited among the three networks. For the total number of atoms in the dangling chains, the LM network has a significantly lower level than the others. Other typical parameters, such as the number of elastic junctions and strands, are found to have insignificant difference among one another. To see if there is more difference in the

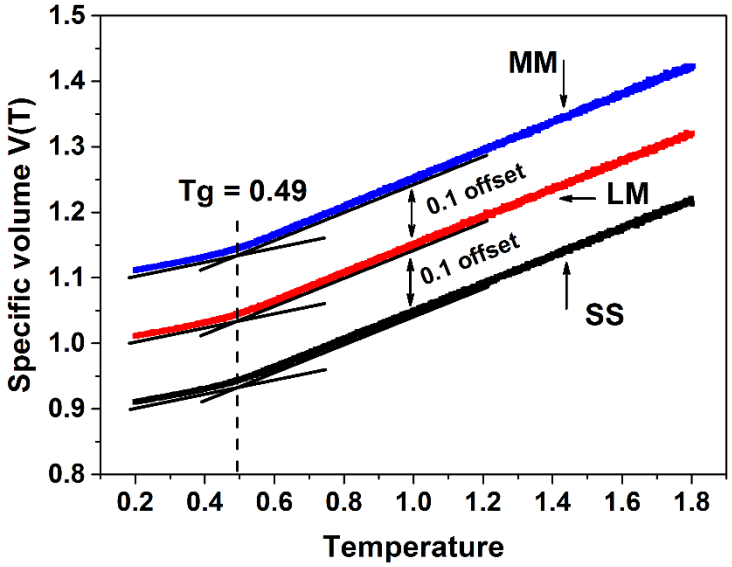

Figure 9.4. Temperature dependence of specific volume in a controlled cooling process.

structural parameters of the final networks, we look into the statistical distribution of elastic strands in terms of their length. **Figure 9.3** shows the probability density function of the strand length (higher lengths are not shown due to their small proportions). In our model, a perfect network is composed of elastic strands with a standard length of 2 (i.e., a bifunctional atom bonded with two elastic junctions). Whereas in actual case, there is a small portion of longer elastic strands which contain one or more elastically inactive junctions (hereafter, these strands will be named as "unsaturated elastic strands" to distinguish from those saturated elastic strands with a length of 2). However, as can be seen from **Figure 9.3**, the three networks have a similar strand length distribution, indicating a similar overall statistics of network connectivity.

For the typical structural parameters shown above, the only difference among the polymer networks formed from the three sets of precursors is total number of dangling atoms. We

then focus on the effects of precursors on the static and dynamic properties of polymer networks which are of common interest, and the relationship between these properties and network structure. We first look at the glass transition temperature (*Tg*) of the polymer networks, which is measured from a controlled cooling process as mentioned above. The results are shown in **Figure 9.4**. In this method, the abrupt change in the specific volume is a typical signature of glass transition, and *Tg* can be determined by intersection of tangents of the two branches which have different slopes in the dilatometric curves.[31] As shown in **Figure 9.4**, the three networks show an almost identical change in the specific volume as temperature decreases, and have a same *Tg* at approximately 0.49. The analogous glass transition behaviors can be attributed to the similar overall network connectivity in all three systems, while the influence of the minor difference in network structure is limited.

9.2 Mechanical Properties

9.2.1 Tensile Deformation

To investigate the mechanical properties of the final networks formed from the three precursors, we perform tensile deformation tests in which the simulation box is subjected to an elongation at a constant true strain rate. The correlation between tensile stress and strain of the polymer networks are shown in **Figure 9.5**. It can be clearly seen that the polymer networks exhibit different stress-strain behaviors. Indeed, the three stress-strain curves begin to diverge from one another at a strain of approximately 0.6, after which the

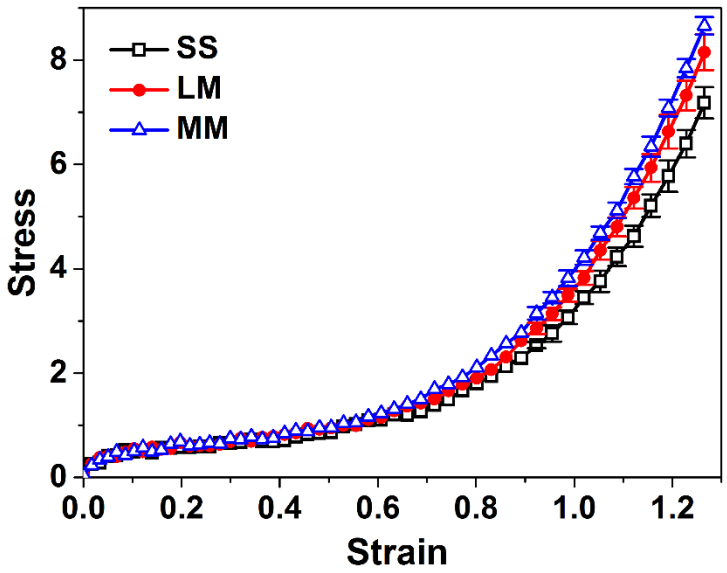

Figure 9.5. Stress-strain curves of the SS, LM and MM networks. Error bars smaller than symbol size are not shown.

highest stress is observed in MM network, while SS network the lowest. Such results suggest that the choice of precursors actually has a strong influence on the elastic modulus of the formed network.

To find out the relationship between elastic modulus of polymer networks and their structure, we first look into a few promising structural parameters which have a strong influence on the mechanical properties of polymer materials. Selected parameters are the number of total bonds, elastic bonds and elastic strands; the results are shown in **Figure 9.6**. Elastic modulus is found to be weakly-correlated with the number of total bonds or number of elastic bonds. Indeed, as can be seen in **Figure 9.6a** and **9.6b**, the chosen structural parameters provide a poor prediction of elastic modulus in which the correlation patterns are also dependent on network systems. A strong correlation can be observed between the modulus and the number of elastic strands as shown in **Figure 9.6c**, which is

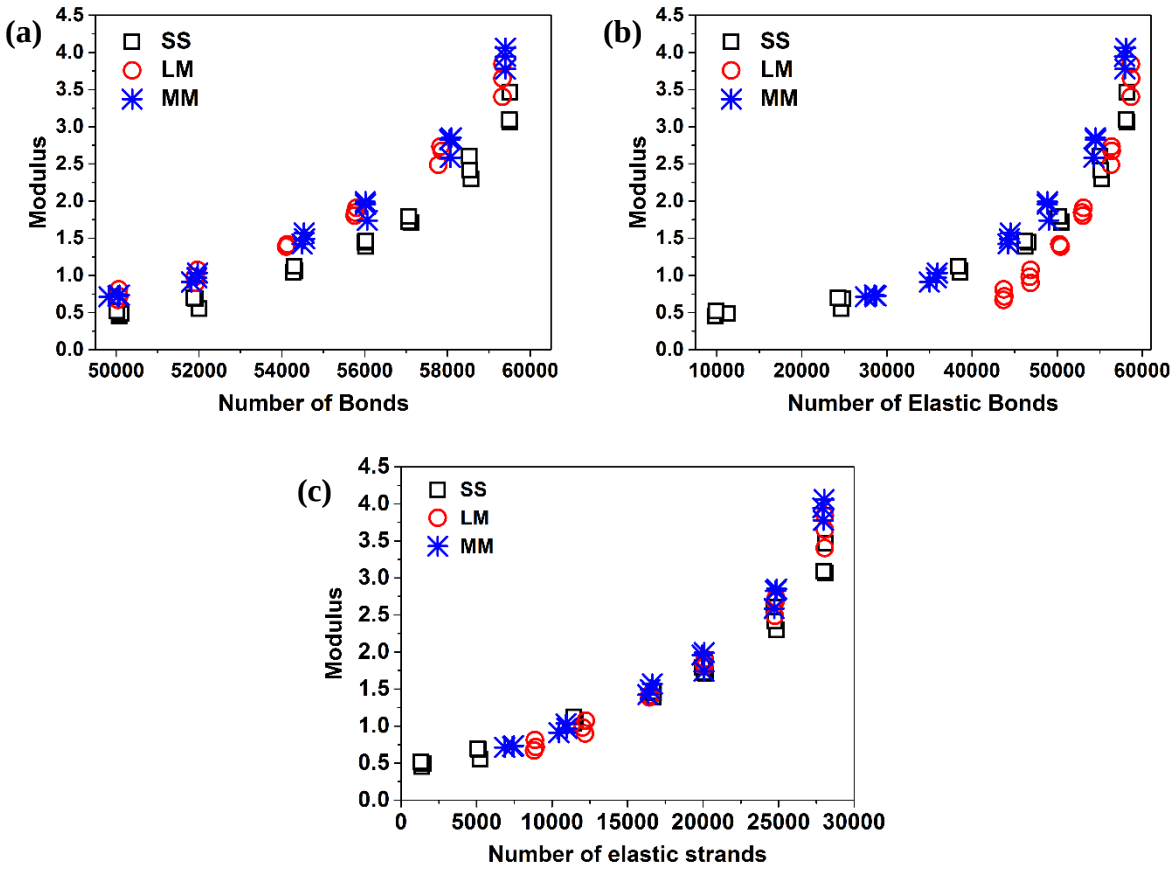

Figure 9.6. Correlation between network elastic modulus and (a) total number of bonds, (b) total number of elastic bonds, and (c) total number of elastic strands.

well-maintained in a broad range. However, a substantial discrepancy between different networks is also observed at the high limit (e.g., final stage with the number of elastic strands at about 28000). As discussed in the following sections, such discrepancy can be understood by looking into more structural parameters which are not commonly characterized.

9.2.2 Spatial Distribution of Structural Defects

As previously discussed in the structure analysis section, the final networks have a similar total number of elastic strands and statistical distributions of strand length. The minor difference in the overall network connectivity cannot explain the discrepancy observed in the relationship between elastic modulus and number of elastic strands. Therefore, we attribute this discrepancy to the presence of structural defects in the polymer networks, which has been considered to have a large influence on mechanical properties of polymer networks in many previous studies.[25, 32] Typically structural defects include dangling chains and single-chain loop with both chain ends connected to an atom. In our trifunctional network, the single-chain loop, if present, has to be on a dangling chain (i.e., dangling loops; free loops are not considered) as the atom it connects to is trifunctional and thus only one end of this strand can be connected to the network. For this reason, we consider such strands as a general type of dangling chains. The structure analysis results show that the final networks have different number of dangling chains/atoms. However, it can be clearly seen that such difference does not correlate to the discrepancy in modulus. Specifically, **Figure 9.5** shows that MM network has the highest modulus, while SS network the lowest. However, MM network actually has a higher level of these defects. This result suggests that the presence of dangling chains/atoms is not the only reason for the different network moduli.

In the other hand, comparing to the atoms in saturated elastic strands, those in unsaturated elastic strands have higher mobility. These atoms can be also considered as one type of structural defects. **Figure 9.7** shows the number of atoms in all structural defects (i.e., dangling and unsaturated strands) in the polymer networks at different stages of formation

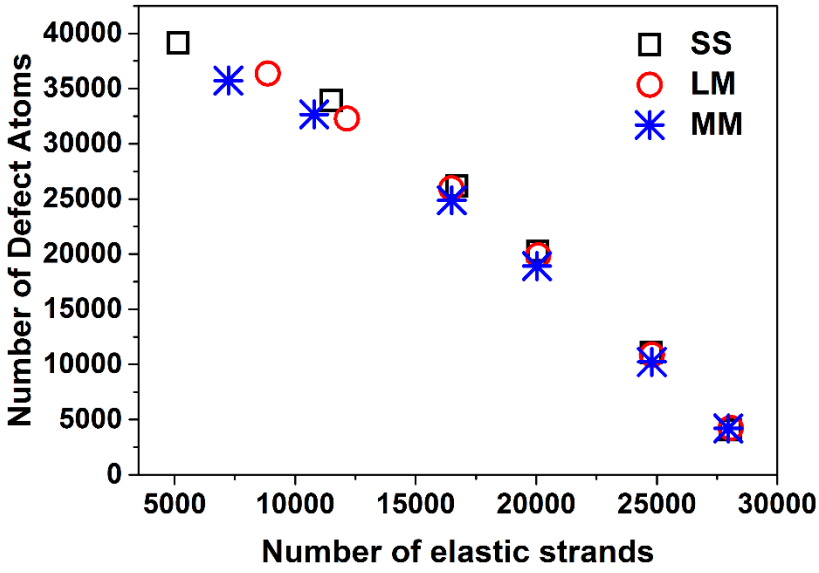

Figure 9.7. Number of structural defect atoms in the polymer networks with varying number of elastic strands. Error bars are not shown due to small values.

process. However, all three networks are found to have a similar level of defects especially at later stages (e.g., when the number of elastic strands is larger than 16000). Clearly the difference in the network modulus shown in **Figure 9.5** does not stem from the number of defects.

These observations prompt us to look into the spatial distributions of structural defects in the polymer networks. As shown in **Figure 9.8**, defects in the three networks have significantly different spatial distributions. Indeed, the defects in SS network show the most homogeneous distribution---they tend to form a bunch of small clusters which are distributed uniformly over the whole simulation box. Whereas in LM network, these defects tend to form larger clusters resulting in an inhomogeneous distribution. Such clustering effect is even stronger in MM network. We then calculate RDF of these particles

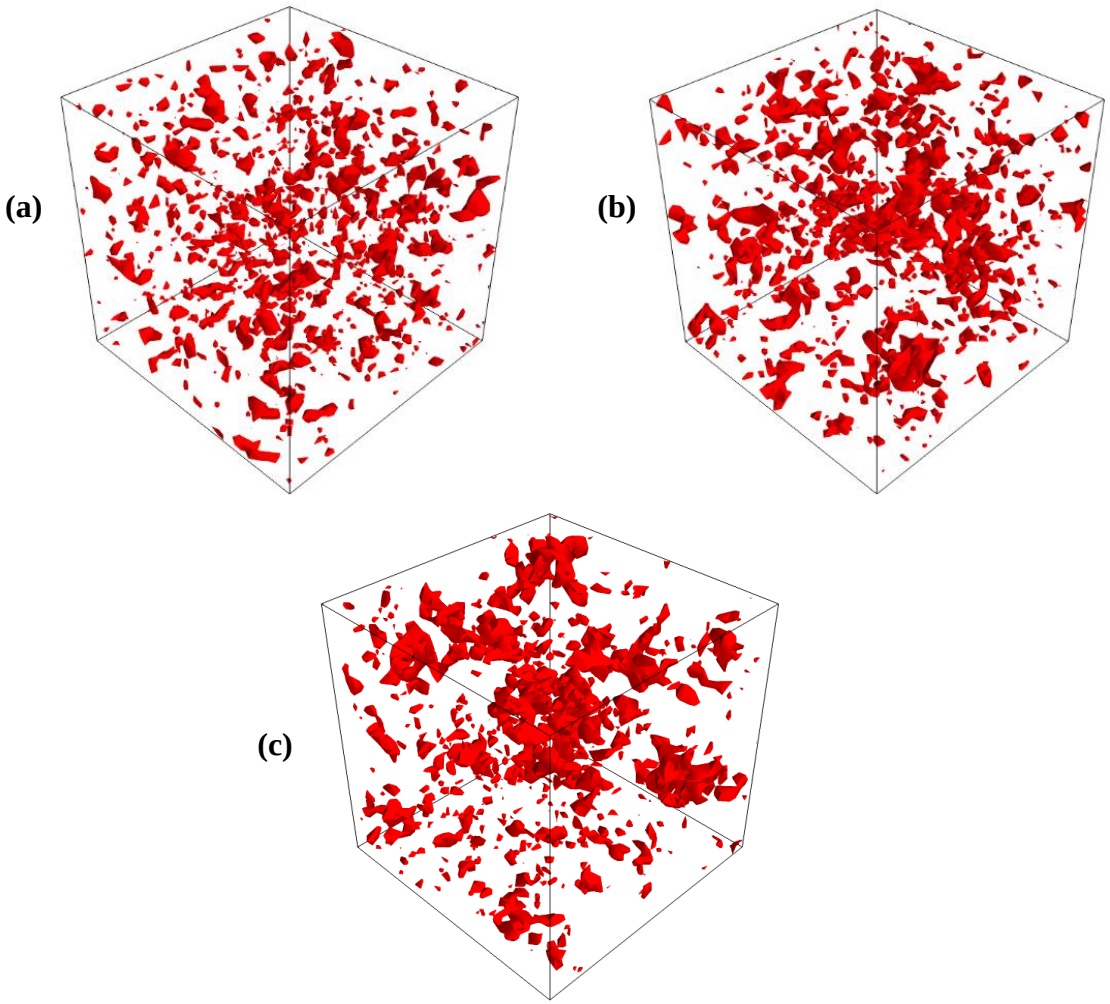

Figure 9.8. Spatial distribution of defects in polymer networks: (a) SS, (b) LM and (c) MM.

to quantify the spatial distribution of defects. The results are presented in **Figure 9.9**. The first peak in RDF is an indication of the local density of particles in the nearest neighbor shell to the reference particle. As can be seen in the figure, the MM network shows the highest first peak, while a lowest peak is observed in SS network. Such result is consistent with that of the 3-dimensional visualization images shown in **Figure 9.8**.

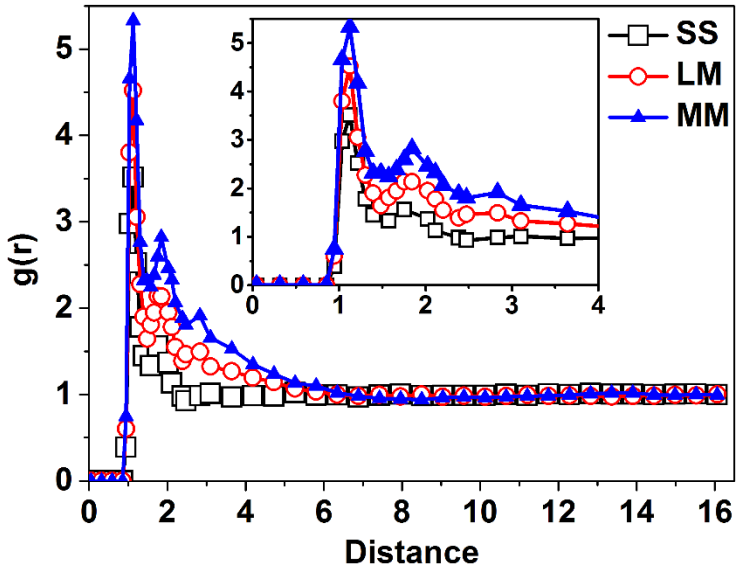

Figure 9.9. Radial distribution function of defect atoms in polymer networks.

The spatial distribution of defects in polymer network can be related to network modulus by comparing our case to particulate-reinforced polymer composites, in which rigid particles with higher modulus are usually used to toughen the polymer matrix. In these composites, dispersion of the reinforcing particles within the polymer matrix is a key factor in determining the toughening effect. It has been established that a well-dispersion of reinforcing particles can lead to better mechanical properties of the polymer-particle composites (e.g., higher modulus and toughness), while a poor dispersion may only make a limited contribution or even worsen the mechanical properties. Contrary to the toughening effect, in polymer networks, the presence of structural defects can instead result in deterioration of the modulus of materials. In this case, these defects can be considered as "weakening particles". Similar to the case in polymer reinforcement, a homogeneous

distribution of these “weakening particles” may maximize the “weakening effect”, and thus results in a lower modulus of the whole network.

To find out the origin that leads to the different spatial distributions of defects in polymer networks, we place our emphasis back to the network formation kinetics. Due to the different chain length of precursors, the three systems involves different gelation processes. The occurrence of gelation is faster in LM system than that in SS and MM systems, as mentioned previously, since it requires much less new bonds to inter-connect long polymer chains to form a network. Therefore, in the early stage of formation process, the formed LM network is quite similar to the initial network composed of physically entangled precursors, and has a homogeneous structure. In the SS and MM systems, however, multiple clusters are formed first through the cross-linking reactions among the small molecules. These clusters keep growing by continuous merging of single precursors and other smaller clusters, and finally form a polymer network when the gelation is triggered. As a result, the newly formed network is an irregular assembly of localized clusters, surrounded by a number of small molecules which have not yet been merged. After the network is formed, removal of structural defects through further cross-linking reactions then becomes the major task of the following process in all three systems.

It is found that the different gelation mechanisms and precursor topologies have a large influence on the homogeneity of network structure. Since defects in the polymer network are actually caused by the presence of unsaturated atoms, their elimination relies on the reactions of these reactive atoms with their unsaturated counterparts nearby. Therefore, the

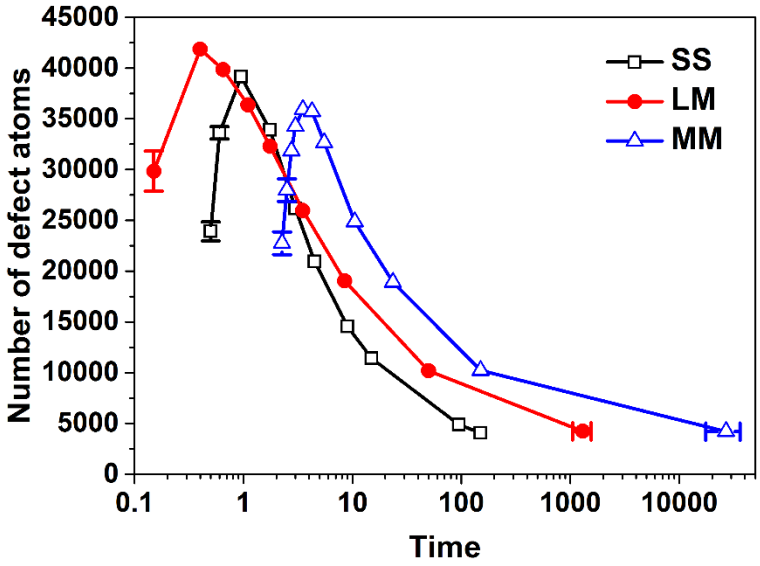

Figure 9.10. Temporal evolution of structural defects in the polymer networks. Error bars smaller than symbol size are not shown.

probability of occurrence of such reaction is largely dependent on the spatial distribution of the reactive atoms. That is, it will be easier for these atoms to meet their counterparts if the distribution is uniform, whereas an inhomogeneous distribution pattern can result in a slower defect elimination process. Moreover, such inhomogeneity can also lead to the formation of spatially localized defect aggregates at late stages of network development, at which most of atoms are connected to network and their mobility are highly restricted. Thus reactive atoms (e.g., unsaturated trifunctional atoms) gathered in one region can hardly react with their counterparts located in other areas, forming permanent defects in the network.

We first study the time evolution of structural defects in the polymer networks after they are formed. As shown in **Figure 9.10**, a rapid increase in the number of defects is involved at early stages, due to a high merging rate of small molecules and/or reactive atoms,

followed by a continuous decay with a decreasing rate. The overall defect removal rates of the three network systems are however substantially different. Indeed, it takes the least time for SS network to remove its defects to a low level (e.g., < 5000), while for MM network, this process is much more time-consuming and requires the longest time period. This result suggests that the defects in MM network are the hardest to be eliminated, while those in SS network may be only temporary and can be removed easily.

These observations can be attributed to spatial distributions of trifunctional and bifunctional atoms within the networks. Due to different gelation mechanisms and precursor topologies, these atoms are distributed with different levels of homogeneity. In MM system, formation of small clusters before the gel point results in an inhomogeneous distribution of the atoms with different functionalities. The trifunctional atoms, as the minor species, are more easily to be reacted (i.e., higher consumption rate) and incorporated into different clusters. We confirm this by counting the number of unreacted bifunctional and trifunctional (i.e., single beads) and find the ratio of these atoms is always beyond the stoichiometric ratio (i.e., 3:2) during the formation process until the single trifunctional atoms are completely depleted. As these clusters are irregularly distributed, there may form regions which are more abundant with one type of reactive atoms while the other type tend to gather in other areas. That is, while composed of a mixture of trifunctional and bifunctional atoms, these regions actually have different compositions (i.e., different ratios of the two types of atoms). Such inhomogeneity eventually results in geographical isolation of reactive atoms which are far apart from each other and are thus difficult to be eliminated. Though clusters are also formed in SS system at the beginning, the distribution of atoms with different

functionalities is still homogeneous because of special topology of the precursor chains. Different from the case in MM system, these clusters are formed by inter-connecting short linear polymer chains in which the bifunctional and trifunctional atoms are bonded with a stoichiometric ratio of 1.5. Hence attachment of one precursor chain to a cluster is equivalent to incorporation of both types of atoms with a constant proportion. Consequently, these atoms are evenly distributed to different clusters, while the distribution patterns of these clusters have little influence on the overall distribution of atoms with different nature. In this sense, the whole SS system can be considered as a regular assembly of bifunctional and trifunctional atoms with growing inter-connections. For LM system, a different gelation mechanism is involved. As discussed earlier, the initial LM network (i.e., after gelation) should have a homogeneous structure similar to the physically entangled precursors chains after equilibration. The cross-linking density of the network at this stage is still low, though almost all precursor chains have been inter-connected with one another. These characteristics indicate that the network actually comprises many cells in which a few long unsaturated strands are connected by elastic junctions. The elimination of structural defects then depends on diffusion of single bifunctional atoms into these cells and form bridges between or within the cell edges. This process can introduce inhomogeneity into network structure in multiple ways. On one hand, a bridge between two unsaturated trifunctional atoms can only be formed when they are sufficiently close to each other. However, this is not always possible for those atoms in the cells which have irregular shapes and various sizes. For the pair of atoms in those large irregular cells, they have a lower probability to successfully form a bridge. Since these cells are placed at different

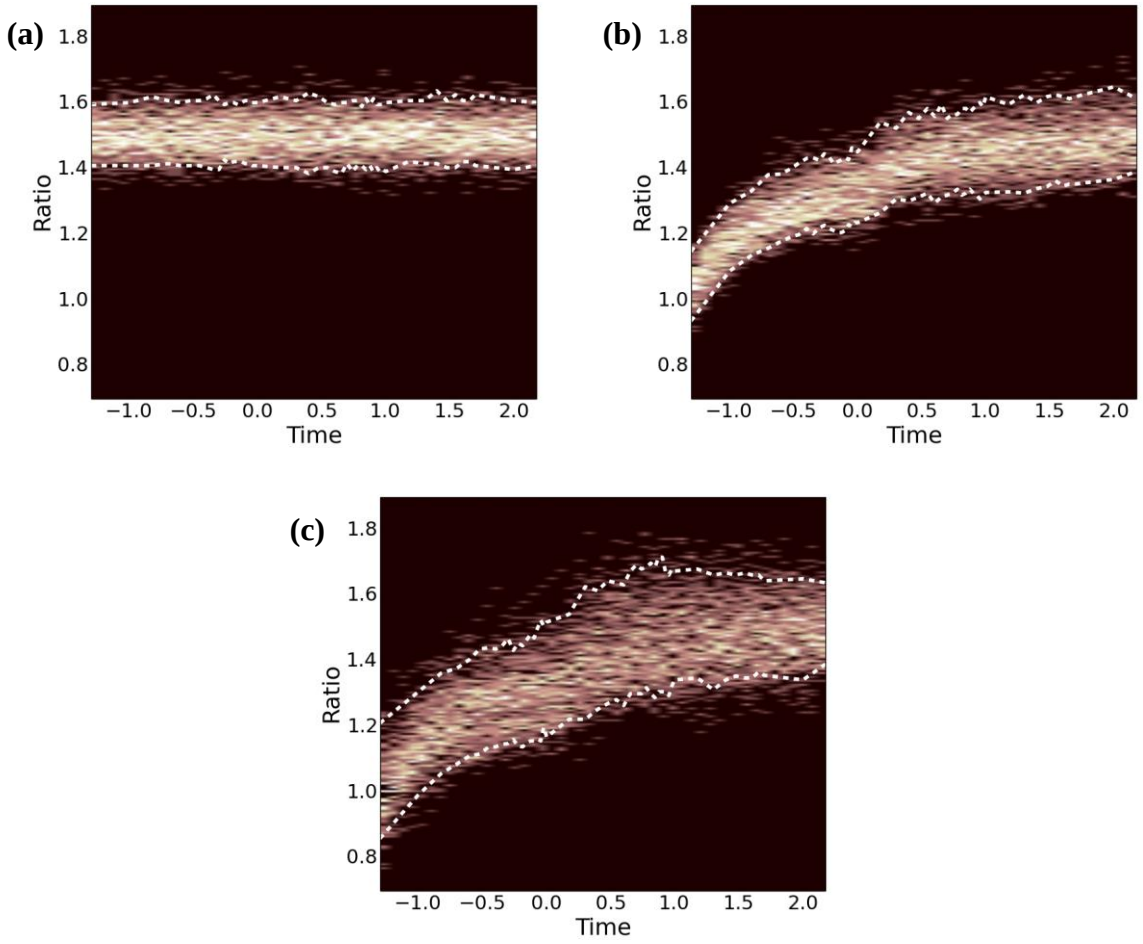

Figure 9.11. Temporal evolution of the probability density function of the ratio of bonded bifunctional and trifunctional atoms in the cells: (a) SS, (b) LM and (c) MM. A logarithmic scale is used for horizontal axis and black indicates vanishing probability. The white dot lines indicate a contour level of 95%.

parts of the network, they will introduce more defects in these areas. On the other hand, these cells may also act as "cages" which entrap the unsaturated strands inside. As a result, it will be difficult for the bifunctional atoms to diffuse into these regions and react with their counterparts, leading to a higher local density of defects.

To confirm the influence of gelation mechanism and precursor topology as stated above, spatial distributions of trifunctional and bifunctional atoms are investigated. Considering that free atoms have much higher mobility than their bonded peers and are randomly distributed, we only look at atoms in all clusters and focus on time evolution of the distributions of these atoms at different regions. The procedure we employ is described as follows: we divide the simulation box into 125 identical cubes and calculate ratio of bifunctional and trifunctional atoms, which are all attached to clusters, within each cell; a time span is chosen from the beginning of cross-linking reaction to a late stage of network development (i.e., time = 150τ when degree of atom saturation is >96% for all three cases). **Figure 9.11** shows the probability density functions (PDFs) of the ratios at different cells as the network formation process proceeds. A narrower band with varied colors is an indication of a more homogeneous distribution of the atoms, as it suggests a smaller variation in the ratios of different cells. As can be seen in **Figure 9.11**, the distributions of bonded bifunctional and trifunctional atoms in SS, LM and MM systems are substantially different from one another. In SS system, little change in the band width is observed over the chosen time span, with the ratios fluctuating around the ideal value of 1.5. Such a constant band width indicates a limited change in distribution profiles during the network formation process. As explained earlier, this result can be attributed to the special topology of short precursor chains. An increasing band width however can be seen in LM system. Due to similar structure between the initial network to physically entangled precursor chains, distributions of bonded bifunctional and trifunctional atoms are fairly homogeneous at early stages, leading to a small deviation of the ratios at different regions. However, as

the network evolves, newly merged bifunctional atoms are not able to be uniformly distributed to different areas for multiple reasons such as the formation of large irregular cells and “cages”. The introduced inhomogeneity can be confirmed by the increasing band width. In MM system, an even more diverging band is observed. The formation of clusters before the gel point significantly changes the local densities of the atoms with different functionalities. Since the mobility of bonded atoms is highly restricted especially after the network is formed, such inhomogeneity can hardly be compensated.

Chapter 10

Conclusions of Part II

Network polymer is an important class of materials that has been a focus in many computational studies. In MD simulations, polymer networks can be virtually synthesized in multiple ways; the influences of these different approaches on the generated polymer networks are however never explored in previous studies. In this work, we focus on the effects of precursor topology on the formation, structure and mechanical properties of polymer networks. Three sets of polymers with varying chain length are used as precursors to prepare networks using MD technique. These precursors are designed in a way that ideally they would form an identical network structure with full conversion. Little difference is found among the final networks in the typically characterized properties, including the radial distribution function, overall network connectivity and glass transition behaviors. To investigate the mechanical properties of these materials, tensile deformation tests are performed in which the simulation box are stretched in both of positive and negative *z* directions, and dynamic response of tensile stress to strain is recorded. It turns out that stress-strain behaviors of the polymer networks are substantially different from one another, indicating a strong dependency of the elastic modulus of the prepared networks on precursor topology. More tensile tests suggest that there is a strong correlation between the total number of elastic strands and the elastic modulus of networks. Such correlation is

found to be independent on the precursor topology in most of network formation process; however, significant deviations are observed at late stages of network development. These differences can be attributed to the presence of structural defects in the polymer networks. Despite of a similar level of defects, the choice of precursor actually has a large influence on spatial distribution of the defect atoms. The most homogeneous distribution is found in SS network, while the defects in MM network tend to form spatially localized clusters and are the least uniform. Relationship between the elastic modulus and distribution of structural defects can be understood by considering the defect atoms as "weakening particles". Contrary to particulate-reinforced polymer composites in which a well-dispersion of particles can lead to a better reinforcement performance, a homogeneous distribution of these "weakening particles" may also maximize the "weakening effect", resulting in a lower elastic modulus. The observed difference in the spatial distributions of structural defects is found to stem from different gelation mechanisms and precursor topologies of the three systems. Due to the special topology of short precursor chains, atoms with different functionalities are able to be distributed uniformly at different regions. The LM system has a quite homogeneous network structure in early stages of formation process. However, for reasons such as the presence of large irregular cells and formation of "cages" which can bury the unsaturated strands inside and reduce their accessibility, free bifunctional atoms cannot form bridges between the two unsaturated trifunctional atoms evenly within the network, resulting in an inhomogeneous structure. In MM system, significant variations are observed in the ratios of the two types of reactive atoms within the multiple clusters formed before gelation. Such inhomogeneity is maintained during the

network formation process, eventually leading to geographical isolation of a small portion of unsaturated reactive atoms, and thus the formation of permanent defect clusters in the final network. These results indicate that the choice of precursors has a substantial impact on the properties of prepared networks, and thus deserves more considerations when developing molecular model of polymer networks using molecular dynamics.

Chapter 11

Future Work

The current MD study provides insights into the formation kinetics, structure and properties of polymer networks. By using precursors with varying chain length, the prepared networks show a substantial difference in the spatial distributions of structural defects and the mechanical properties measured in tensile deformation tests. We thus confirm the precursor dependency of the development of molecular model of polymer networks. Our next step is to use the appropriate model to answer the fundamental questions raised from our experimental observations. We have shown in the Part I of this thesis that the performance of the resin coatings (i.e., cross-linked phenolic resin) is dependent on the temperature and process time, and the coating process involves complex coupling of multiple physical and chemical processes. We are particularly interested in using the MD technique to reveal the competition profile of these underlying processes and how the profile is influenced by temperature. The influence of these simultaneous processes on the properties of the prepared polymer networks can also be systematically studied by MD simulations. Eventually, the understandings we acquire from such studies can aid us in controlling the multiple operating conditions and thus contribute to the experimental design of network polymers for a broader range of applications.

Another issue of interest to us is the domain size effect on the formation, structure and properties of polymer networks. The current system size of the simulations is only limited to 50000 particles, which does not allow us to observe the behaviors of polymer systems at a macroscopic level. However, by resorting to the advanced high performance computing (HPC) power, we now have access to much larger scales and MD simulations with a system size of up to millions of particles are possible. Our interest in such a large scale of simulation stems from the experimental observations[3] that the formation of polymer networks, when prepared by cross-linking bi- and multifunctional monomers, actually involves formation of multiple nanogels localized in different regions before macroscopic gelation takes place. The final network then is a loose assembly of these nanogels, resulting in an inhomogeneous spatial distribution of cross-links. Such phenomenon is not observed in our current simulation study---while we do find that in MM system, multiple small clusters are formed first before gelation, final network does not have a higher local density variation (i.e., RDF with higher peaks) compared to the other two cases, but instead show a similar homogeneity in the overall network structure (**Figure 9.2**). However, by extending our simulations to a much larger scale, we probably will be able to capture these features and many other characteristics of the polymer network systems which are not well-studied in simulations. Most of previous computational studies are limited to a microscopic level similar to our current settings, we believe our trials in the scales of systems up to a macroscopic level can provide new insights into the simulations of polymer networks.

Bibliography

(1) Aharoni, S. M. *Synthesis, characterization, and theory of polymeric networks and gels*; Springer, 1992.

(2) Dusek, K.; Kuchanov, S. I. *Polymer Networks*; CRC Press, 1992.

(3) Seiffert, S.; Sprakel, J. Physical chemistry of supramolecular polymer networks. *Chemical Society Reviews* **2012**, *41*, 909.

(4) Nouri, N.; Ziaei-Rad, S. A molecular dynamics investigation on mechanical properties of cross-linked polymer networks. *Macromolecules* **2011**, *44*, 5481.

(5) Varshney, V.; Patnaik, S. S.; Roy, A. K.; Farmer, B. L. A molecular dynamics study of epoxy-based networks: cross-linking procedure and prediction of molecular and material properties. *Macromolecules* **2008**, *41*, 6837.

(6) Krumova, M.; Lopez, D.; Benavente, R.; Mijangos, C.; Perena, J. Effect of crosslinking on the mechanical and thermal properties of poly (vinyl alcohol). *Polymer* **2000**, *41*, 9265.

(7) Yagyu, H.; Utsumi, T. Coarse-grained molecular dynamics simulation of nanofilled crosslinked rubber. *Computational Materials Science* **2009**, *46*, 286.

(8) Wu, C.; Xu, W. Atomistic molecular modelling of crosslinked epoxy resin. *Polymer* **2006**, *47*, 6004.

(9) Izumi, A.; Nakao, T.; Shibayama, M. Atomistic molecular dynamics study of cross-linked phenolic resins. *Soft Matter* **2012**, *8*, 5283.

(10) Binder, K. *Monte Carlo and molecular dynamics simulations in polymer science*; Oxford University Press, 1995.

(11) Grest, G. S.; Kremer, K. Molecular dynamics simulation for polymers in the presence of a heat bath. *Physical Review A* **1986**, *33*, 3628.

(12) Kremer, K.; Grest, G. S. Dynamics of entangled linear polymer melts: A molecular-dynamics simulation. *The Journal of Chemical Physics* **1990**, *92*, 5057.

(13) Milchev, A.; Binder, K. Static and dynamic properties of adsorbed chains at surfaces: Monte Carlo simulation of a bead-spring model. *Macromolecules* **1996**, *29*, 343.

(14) Leung, Y. K.; Eichinger, B. Computer simulation of end-linked elastomers. I. Trifunctional networks cured in the bulk. *The Journal of Chemical Physics* **1984**, *80*, 3877.

(15) Leung, Y. K.; Eichinger, B. Computer simulation of end-linked elastomers. II. Bulk cured tetrafunctional networks. *The Journal of Chemical Physics* **1984**, *80*, 3885.

(16) Duering, E. R.; Kremer, K.; Grest, G. S. Dynamics of model networks: the role of the melt entanglement length. *Macromolecules* **1993**, *26*, 3241.

(17) Duering, E. R.; Kremer, K.; Grest, G. S. Structure and relaxation of end-linked polymer networks. *The Journal of Chemical Physics* **1994**, *101*, 8169.

(18) Grest, G. S.; Kremer, K.; Duering, E. R. Kinetics and relaxation of end crosslinked polymer networks. *Physica A: Statistical Mechanics and Its Applications* **1993**, *194*, 330.

(19) Tsige, M.; Lorenz, C. D.; Stevens, M. J. Role of network connectivity on the mechanical properties of highly cross-linked polymers. *Macromolecules* **2004**, *37*, 8466.

(20) Yang, W.; Wei, D.; Jin, X.; Liao, Q. Molecular dynamics simulation of the formation of polymer networks. *Macromolecular Theory and Simulations* **2007**, *16*, 548.

(21) Hosono, N.; Masubuchi, Y.; Furukawa, H.; Watanabe, T. A molecular dynamics simulation study on polymer networks of end-linked flexible or rigid chains. *The Journal of Chemical Physics* **2007**, *127*, 164905.

(22) Svaneborg, C.; Grest, G. S.; Everaers, R. Disorder effects on the strain response of model polymer networks. *Polymer* **2005**, *46*, 4283.

(23) Rottach, D. R.; Curro, J. G.; Budzien, J.; Grest, G. S.; Svaneborg, C.; Everaers, R. Permanent set of cross-linking networks: Comparison of theory with molecular dynamics simulations. *Macromolecules* **2006**, *39*, 5521.

(24) Rottach, D. R.; Curro, J. G.; Budzien, J.; Grest, G. S.; Svaneborg, C.; Everaers, R. Molecular dynamics simulations of polymer networks undergoing sequential cross-linking and scission reactions. *Macromolecules* **2007**, *40*, 131.

(25) Sliozberg, Y. R.; Chantawansri, T. L. Computational study of imperfect networks using a coarse-grained model. *The Journal of Chemical Physics* **2013**, *139*, 194904.

(26) Tsige, M.; Stevens, M. J. Effect of cross-linker functionality on the adhesion of highly cross-linked polymer networks: a molecular dynamics study of epoxies. *Macromolecules* **2004**, *37*, 630.

(27) Auhl, R.; Everaers, R.; Grest, G. S.; Kremer, K.; Plimpton, S. J. Equilibration of long chain polymer melts in computer simulations. *The Journal of Chemical Physics* **2003**, *119*, 12718.

(28) Sliozberg, Y. R.; Andzelm, J. W. Fast protocol for equilibration of entangled and branched polymer chains. *Chemical Physics Letters* **2012**, *523*, 139.

(29) Duering, E.; Kremer, K.; Grest, G. Structural properties of randomly crosslinked polymer networks. In *Physics of Polymer Networks*; Springer; 1992. pp 13.

(30) Herrmann, H.; Hong, D.; Stanley, H. Backbone and elastic backbone of percolation clusters obtained by the new method of 'burning'. *Journal of Physics A: Mathematical and General* **1984**, *17*, L261.

(31) Askadskiĭ, A. A. *Computational materials science of polymers*; Cambridge Int Science Publishing, 2003.

(32) Larsen, A. L.; Hansen, K.; Sommer-Larsen, P.; Hassager, O.; Bach, A.; Ndoni, S.; Jørgensen, M. Elastic properties of nonstoichiometric reacted PDMS networks. *Macromolecules* **2003**, *36*, 10063.